Joint Analysis of Cluster Observations. II. Chandra/XMM-Newton X-Ray and Weak Lensing Scaling Relations for a Sample of 50 Rich Clusters of Galaxies

Mahdavi, A.; Hoekstra, H.; Babul, A.; Bildfell, C.; Jeltema, T.; Henry, J.

The Astrophysical Journal, 767:116 (18pp), 2013 April 20 doi:10.1088/0004-637X/767/2/116

JOINT ANALYSIS OF CLUSTER OBSERVATIONS. II. *CHANDRA*/*XMM-NEWTON* X-RAY AND WEAK LENSING SCALING RELATIONS FOR A SAMPLE OF 50 RICH CLUSTERS OF GALAXIES

Andisheh Mahdavi[1], Henk Hoekstra[2], Arif Babul[3], Chris Bildfell[3], Tesla Jeltema[4], and J. Patrick Henry[5]
[1] Department of Physics and Astronomy, San Francisco State University, San Francisco, CA 94131, USA
[2] Leiden Observatory, Leiden University, Niels Bohrweg 2, NL-2333 CA Leiden, The Netherlands
[3] Department of Physics and Astronomy, University of Victoria, Victoria, BC V8W 3P6, Canada
[4] Santa Cruz Institute for Particle Physics, UC Santa Cruz, 1156 High Street, Santa Cruz, CA 95064, USA
[5] Institute for Astronomy, 2680 Woodlawn Drive, Honolulu, HI 96822, USA
Received 2012 October 12; accepted 2013 February 25; published 2013 April 3

ABSTRACT

We present a study of multiwavelength X-ray and weak lensing scaling relations for a sample of 50 clusters of galaxies. Our analysis combines *Chandra* and *XMM-Newton* data using an energy-dependent cross-calibration. After considering a number of scaling relations, we find that gas mass is the most robust estimator of weak lensing mass, yielding $15\% \pm 6\%$ intrinsic scatter at $r_{500}^{\rm WL}$ (the pseudo-pressure Y_X yields a consistent scatter of $22\% \pm 5\%$). The scatter does not change when measured within a fixed physical radius of 1 Mpc. Clusters with small brightest cluster galaxy (BCG) to X-ray peak offsets constitute a very regular population whose members have the same gas mass fractions and whose even smaller ($<10\%$) deviations from regularity can be ascribed to line of sight geometrical effects alone. Cool-core clusters, while a somewhat different population, also show the same ($<10\%$) scatter in the gas mass–lensing mass relation. There is a good correlation and a hint of bimodality in the plane defined by BCG offset and central entropy (or central cooling time). The pseudo-pressure Y_X does not discriminate between the more relaxed and less relaxed populations, making it perhaps the more even-handed mass proxy for surveys. Overall, hydrostatic masses underestimate weak lensing masses by 10% on the average at $r_{500}^{\rm WL}$; but cool-core clusters are consistent with no bias, while non-cool-core clusters have a large and constant 15%–20% bias between $r_{2500}^{\rm WL}$ and $r_{500}^{\rm WL}$, in agreement with *N*-body simulations incorporating unthermalized gas. For non-cool-core clusters, the bias correlates well with BCG ellipticity. We also examine centroid shift variance and power ratios to quantify substructure; these quantities do not correlate with residuals in the scaling relations. Individual clusters have for the most part forgotten the source of their departures from self-similarity.

Key words: galaxies: clusters: general – galaxies: clusters: intracluster medium – gravitational lensing: weak – X-rays: galaxies: clusters

Online-only material: color figures

1. INTRODUCTION

Within the context of the currently favored hierarchical model for structure formation, massive clusters of galaxies are, as a population, the most recently formed gravitationally bound structures in the cosmos. Consequently, characteristics such as the shape and evolutionary behavior of their mass function can, in principle, be exploited as precision probes of cosmology. The resulting estimates of parameters—such as the amplitude of the primordial fluctuations and the density and equation of state of the mysterious dark energy—can certainly complement and even compete with determinations based on studies of the cosmic microwave background (for a review see Allen et al. 2011).

The efficacy of clusters as cosmological probes depends on three factors: (1) the ability to compile a large well-understood catalog of clusters; (2) the identification of an easily determined survey observable (or combinations thereof)—hereafter referred to as a "mass proxy"—that can offer an accurate measure of cluster masses; and (3) the existence of a well-calibrated relationship between the mass proxy and the actual mass of the cluster. Of these, we shall focus our attention on the latter two since at present, the effective use of clusters as cosmological probes is primarily limited by systematic errors in the estimates of the true mass of the cluster (Henry et al. 2009; Vikhlinin et al. 2009b; Mantz et al. 2010).

One of the first—and still among the most commonly used—mass proxies is the "hydrostatic mass estimate," derived from X-ray observations under the assumption that the clusters are spherically symmetric and that the hot, diffuse, X-ray emitting gas in galaxy clusters is in thermal pressure-supported hydrostatic equilibrium (HSE). Over the years, mismatches between hydrostatic mass estimates and mass estimates derived by alternate means have led a number of researchers to question the use of this proxy (e.g., Miralda-Escude & Babul 1995; Fischer & Tyson 1997; Girardi et al. 1997; Ota et al. 2004). Recent studies suggest that the HSE masses of relaxed clusters are subject to a systematic 10%–20% underestimate which grows to 30% or more for unrelaxed systems (Arnaud et al. 2007; Mahdavi et al. 2008; Lau et al. 2009). Numerical simulation studies suggest that this bias is due to incomplete thermalization of the hot diffuse intracluster medium (ICM) (Evrard 1990; Rasia et al. 2006; Nagai et al. 2007; Shaw et al. 2010; Rasia et al. 2012).

Concerns with the HSE mass estimate have renewed interest in identifying more well-behaved mass proxies that can give unbiased estimates of the cluster mass. One example of such an X-ray mass proxy is Y_X, the product of the gas mass M_g and ICM temperature T_X within a given aperture (Kravtsov et al. 2006). In numerical simulation studies, this pressure-like quantity has been shown be a much better mass proxy and has been successfully deployed in measurements of cosmological parameters including the dark energy equation of state (Vikhlinin et al.

2009a, 2009b). More recently, the gas mass M_g has also emerged as a mass proxy with similar predictive power to Y_X (Okabe et al. 2010; Allen et al. 2011). Success in tests involving simulated clusters is necessary but far from sufficient. At present, numerically simulated clusters capture only a fraction of the physical processes that affect the ICM in real clusters.

An alternative way of independently testing the validity of the individual mass proxies is via multiwavelength observations. Specifically, comparisons of X-ray proxies and weak gravitational lensing masses (M_L) are particularly interesting given the fact that gravitational lensing provides a *total* mass estimate that neither depends on baryonic physics nor requires any strong assumptions about the equilibrium state of the gas and dark matter, and which can be determined over a wide range of spatial scales. However, lensing measures the projected (2D) mass and converting this to an unprojected (3D) mass has the effect of adding an amount of scatter that is related to the geometry of the mass distribution, its orientation along the line of sight, and projection of extra-cluster mass along the line of sight (Rasia et al. 2012). In extreme cases, these effects can result in an under- or overestimate of the cluster mass of as much as a factor of two (Feroz & Hobson 2012), depending on the specific technique used.

In this work, we employ a technique that achieves a low systematic weak lensing mass bias of 3%–4%, thanks to the procedure described in detail in Hoekstra et al. (2012). This bias level is lower than the 5%–10% that is usual for numerical simulations, which also have a typical scatter of 20%–30% (Becker & Kravtsov 2011; Bahé et al. 2012; Rasia et al. 2012; High et al. 2012); the actual amount of bias depends on the range of physical radii used in the weak lensing analysis.

At any rate, weak lensing masses are, at present, the best measures of cluster mass and very well suited for use in calibrating the different mass proxies and identifying the best one of the lot. Moreover, the study of the relationship between the weak lensing mass estimate and an observable mass proxy can potentially yield important insights into the physics at play within cluster environments. These are the goals of the present paper.

To facilitate our study, we have assembled a sample of galaxy clusters named the Canadian Cluster Comparison Project (CCCP).[6] We describe this sample in Section 2. In the present study, we restrict ourselves to studying the relationships between weak lensing mass determinations and the mass proxies derived jointly from *Chandra* and *XMM-Newton* observations. We use the Joint Analysis of Observations (JACO) code base (Mahdavi et al. 2007) to derive the mass proxies of interest from the X-ray data. JACO makes maximal use of the available data while incorporating detailed corrections for instrumental effects (for example, we model spatial and energy variations of the point-spread function (PSF) for both *Chandra* and *XMM-Newton*) to yield self-consistent radial profiles for both the dark and the baryonic components. Further details are given in Section 2.4. In Section 2 we summarize our data reduction procedure; in Section 2.4 we describe our mass modeling technique. Our quantitative measures of substructure, the luminosity–temperature relation, the lensing mass–observable relations, and deviations from HSE are discussed in Section 3, Section 4, Section 5, and Section 6, respectively. We conclude in Section 7. Throughout the paper we take $H_0 = 70\ \mathrm{km\ s^{-1}\ Mpc^{-1}}$, $\Omega_M = 0.3$, and $\Omega_\Lambda = 0.7$.

[6] Not to be confused with the Chandra Cluster Cosmology Project (Vikhlinin et al. 2009b), which forms an identical acronym.

2. SAMPLE AND DATA REDUCTION

2.1. Sample Characterization

The CCCP was established primarily to study the different baryonic tracers of cluster mass and to explore insights about the thermal properties of the hot diffuse gas and the dynamical states of the clusters that can be gained from cluster-to-cluster variations in these relationships.

For this purpose, we assembled a sample of 50 clusters of galaxies in the redshift range $0.15 < z < 0.55$. Since we wanted to carry out a weak lensing analysis, we required that the clusters be observable from the Canada–France–Hawaii Telescope (CFHT) so we could take advantage of the excellent capabilities of this facility. The latter constraint restricts our cluster sample to systems at $-15^\circ <$ declination $< 65^\circ$. We also required our clusters to have an *ASCA* temperature $k_B T_X > 3$ keV. To establish cluster temperature, we primarily relied on a systematically reduced cluster catalog of Horner (2001) based on *ASCA* archival data, although in a few instances we used temperatures from other (published) sources.

As a starting point, we scoured the CFHT archives for clusters with high-quality optical data suitable for weak lensing analysis, including observations in two bands. We identified 20 suitable clusters observed with the CFH12k camera and with B and R band data meeting our criteria. Nearly half of these clusters were originally observed as part of the Canadian Network for Observational Cosmology (CNOC1) Survey (Yee et al. 1996; Carlberg et al. 1996) and comprise the brightest clusters in the *Einstein Observatory* Extended Medium Sensitivity Survey (EMSS; Gioia et al. 1990). Since the EMSS sample is known to have a mild bias against X-ray luminous clusters with pronounced substructure (Pesce et al. 1990; Donahue et al. 1992; Ebeling et al. 2000), and we were specifically interested in putting together a representative sample of clusters that encompassed the spectrum of observed variations in thermal and dynamical states, we randomly selected 30 additional clusters from the Horner sample that met our temperature, declination, and redshift constraints and additionally, guaranteed that our final sample fully sampled the scatter in the L_X versus T_X plane. Of these systems, those without deep, high-quality optical data were observed with the CFHT MegaCam wide-field imager, using the g' and r' optical filter sets. The resulting weak lensing masses for this sample are discussed in Hoekstra et al. (2012).

Our final sample comprises 50 clusters listed in Table 1. All except three clusters have been observed by the *Chandra Observatory*. These three, plus 21 others, have also been observed by *XMM-Newton*. Subsets of the CCCP cluster sample have been used in several prior studies (Hoekstra 2007; Mahdavi et al. 2008; Bildfell et al. 2008, 2012). The CCCP sample has served as the source for studies of individual clusters that are interesting in their own right, such as A520 and IRAS 09104+4109 (Mahdavi et al. 2007; Jee et al. 2012; O'Sullivan et al. 2012).

In the left panel of Figure 1, we compare the distribution of the CCCP clusters in the L_X–T_X plane to those of two better characterized samples of galaxies clusters: MACS (Ebeling et al. 2010) and HIFLUGCS (Reiprich & Böhringer 2002), both of which employ well-defined flux-based selection criteria based on the *ROSAT* All-Sky Survey. HIFLUGCS is on the average a lower redshift sample compared to our CCCP sample, and MACS is on the average at a higher redshift. The samples have comparable scatter, suggesting that our CCCP sample is not significantly more biased than HIFLUGCS or MACS,

Table 1
Basic Properties of the Sample

Cluster Name	R.A. J2000	Decl. J2000	z	*Chandra* ObsID	Exposure (s)	*XMM-Newton* ObsID	Exposure (s)	$L_{\rm X,all,bol,500}$ (10^{45} erg s^{-1})	$T_{\rm all,500}$ (keV)
3C295	14:11:20.52	+52:12:09.9	0.464	2254	87914	···	···	1.77 ± 0.06	5.9 ± 0.6
A0068	00:37:06.65	+09:09:24.0	0.255	3250	9986	0084230201	14068	1.87 ± 0.05	6.8 ± 0.4
A0115N	00:55:50.37	+26:24:36.6	0.197	3233	49719	0203220101	21393	1.00 ± 0.01	5.2 ± 0.1
A0115S	00:56:00.17	+26:20:29.5	0.197	3233	49719	0203220101	21309	0.68 ± 0.02	5.5 ± 0.3
A0209	01:31:53.42	−13:36:46.3	0.206	3579	9986	0084230301	11219	1.86 ± 0.03	7.0 ± 0.3
A0222	01:37:34.25	−12:59:30.8	0.207	4967	45078	0502020201	23178	0.50 ± 0.02	4.1 ± 0.3
A0223S	01:37:56.06	−12:49:12.8	0.207	4967	45078	0502020201	23206	0.48 ± 0.01	5.6 ± 0.3
A0267	01:52:42.38	+01:00:48.0	0.231	3580	19624	0084230401	10421	1.47 ± 0.04	6.8 ± 0.3
A0370	02:39:53.18	−01:34:34.9	0.375	515	68532	···	···	1.89 ± 0.05	7.4 ± 0.6
A0383	02:48:03.33	−03:31:45.1	0.187	2320	19285	0084230501	20237	1.51 ± 0.01	3.9 ± 0.1
A0520	04:54:10.10	+02:55:18.3	0.199	4215	66274	0201510101	21915	1.75 ± 0.04	7.8 ± 0.4
A0521	04:54:06.30	−10:13:16.9	0.253	901	38626	···	···	1.09 ± 0.03	5.9 ± 0.3
A0586	07:32:20.16	+31:37:56.6	0.171	530	10043	···	···	1.62 ± 0.06	5.4 ± 0.4
A0611	08:00:56.96	+36:03:22.0	0.288	3194	36114	···	···	1.94 ± 0.06	7.0 ± 0.9
A0697	08:42:57.29	+36:21:56.2	0.282	4217	19516	···	···	3.32 ± 0.10	10.0 ± 1.1
A0851	09:43:00.39	+46:59:20.4	0.407	···	···	0106460101	15731	0.91 ± 0.03	5.7 ± 0.5
A0959	10:17:35.61	+59:33:53.4	0.286	···	···	0406630201	4134	0.74 ± 0.04	6.5 ± 1.7
A0963	10:17:03.63	+39:02:48.3	0.206	903	36289	0084230701	17234	1.96 ± 0.04	6.2 ± 0.2
A1689	13:11:29.52	−01:20:29.8	0.183	6930	76144	0093030101	24457	4.91 ± 0.02	9.1 ± 0.2
A1758E	13:32:46.43	+50:32:25.9	0.279	2213	55220	···	···	1.70 ± 0.03	9.6 ± 0.9
A1758W	13:32:38.70	+50:33:23.0	0.279	2213	55220	···	···	1.30 ± 0.03	9.9 ± 1.4
A1763	13:35:18.16	+40:59:57.7	0.223	3591	19595	0084230901	8852	2.01 ± 0.04	7.0 ± 0.3
A1835	14:01:01.90	+02:52:42.7	0.253	6880	117918	0098010101	16021	7.00 ± 0.03	7.0 ± 0.1
A1914	14:26:02.80	+37:49:27.3	0.171	3593	18865	0112230201	17025	3.61 ± 0.06	9.3 ± 0.3
A1942	14:38:21.90	+03:40:12.9	0.224	3290	55716	···	···	0.44 ± 0.02	4.4 ± 0.5
A2104	15:40:08.09	−03:18:16.5	0.153	895	49199	···	···	1.62 ± 0.02	5.9 ± 0.3
A2111	15:39:41.74	+34:25:01.9	0.229	544	10299	···	···	1.13 ± 0.04	6.0 ± 1.0
A2163	16:15:46.05	−06:09:02.6	0.203	1653	71148	···	···	5.95 ± 0.10	11.0 ± 0.4
A2204	16:32:46.92	+05:34:32.4	0.152	7940	77141	0306490201	13093	5.34 ± 0.02	7.1 ± 0.2
A2218	16:35:50.89	+66:12:36.9	0.176	1666	30693	0112980101	13111	1.70 ± 0.02	6.8 ± 0.2
A2219	16:40:20.20	+46:42:35.3	0.226	896	42295	···	···	4.66 ± 0.08	8.9 ± 0.6
A2259	17:20:07.75	+27:40:14.7	0.164	3245	9986	···	···	1.00 ± 0.07	5.3 ± 0.6
A2261	17:22:27.12	+32:07:58.9	0.224	5007	24316	···	···	3.29 ± 0.09	6.4 ± 0.5
A2390	21:53:36.82	+17:41:44.7	0.228	4193	93782	0111270101	8100	5.39 ± 0.03	8.8 ± 0.2
A2537	23:08:22.23	−02:11:30.3	0.295	4962	36193	0205330501	6267	1.78 ± 0.06	6.8 ± 0.7
CL0024.0+1652	00:26:35.94	+17:09:46.2	0.390	929	39417	···	···	0.49 ± 0.03	4.6 ± 1.1
MACSJ0717.5+3745	07:17:31.39	+37:45:24.8	0.548	4200	58912	···	···	6.08 ± 0.15	11.3 ± 1.0
MACSJ0913.7+4056	09:13:45.49	+40:56:28.7	0.442	10445	76159	···	···	3.18 ± 0.04	6.0 ± 0.3
MS0015.9+1609	00:18:33.74	+16:26:09.0	0.541	520	67410	0111000101	22477	4.22 ± 0.08	8.7 ± 0.7
MS0440.5+0204	04:43:09.99	+02:10:19.3	0.190	4196	22262	···	···	0.59 ± 0.03	3.4 ± 0.4
MS0451.6-0305	04:54:11.24	−03:00:57.3	0.550	902	43420	···	···	3.96 ± 0.12	10.2 ± 1.2
MS0906.5+1110	09:09:12.73	+10:58:28.4	0.174	924	29752	···	···	1.07 ± 0.04	5.5 ± 0.3
MS1008.1−1224	10:10:32.52	−12:39:53.1	0.301	926	25222	···	···	1.11 ± 0.04	5.8 ± 0.6
MS1231.3+1542	12:33:55.01	+15:26:02.3	0.233	···	···	0404120101	26520	0.34 ± 0.01	4.6 ± 0.4
MS1358.1+6245	13:59:50.56	+62:31:05.3	0.328	516	50989	···	···	1.69 ± 0.04	6.6 ± 0.6
MS1455.0+2232	14:57:15.05	+22:20:33.2	0.258	4192	91626	0108670201	22571	3.14 ± 0.02	4.4 ± 0.1
MS1512.4+3647	15:14:22.47	+36:36:20.9	0.372	800	36400	···	···	0.78 ± 0.03	3.1 ± 0.3
MS1621.5+2640	16:23:35.05	+26:34:22.1	0.426	546	30062	···	···	1.03 ± 0.07	6.5 ± 1.4
RXJ1347.5−1145	13:47:30.59	−11:45:09.8	0.451	3592	57458	0112960101	21712	13.15 ± 0.22	12.1 ± 0.4
RXJ1524.6+0957	15:24:38.85	+09:57:41.8	0.520	1664	49849	···	···	0.48 ± 0.04	5.1 ± 1.0

Note. $L_{\rm X,all,bol,500}$ is the bolometric X-ray luminosity and $T_{\rm all,500}$ is the temperature measured using all data within $r_{500}^{\rm WL}$ of the cluster center.

which have better understood selection functions. In the right panel of Figure 1, we plot the distribution of the orthogonal scatter about the mean L_X–T_X of all three samples combined. A K-S test indicates that the three distributions are statistically indistinguishable. This confirms that while the CCCP sample may not be a complete sample, it is a representative sample in that it properly captures the scatter in the L_X–T_X and, to the extent that these have physical origins, the range of cluster thermal and dynamical states.

2.2. Choice of Density Contrast

For most of what follows, we study masses, temperatures, substructure measures, and other thermodynamic quantities integrated within a specific spherical radius. The choice of this radius is not obvious; using fixed physical radii has the advantage of straightforwardness, but the disadvantage that we would be probing characteristically different regions of clusters as a function of masses. Using fixed overdensity radii r_Δ (defined

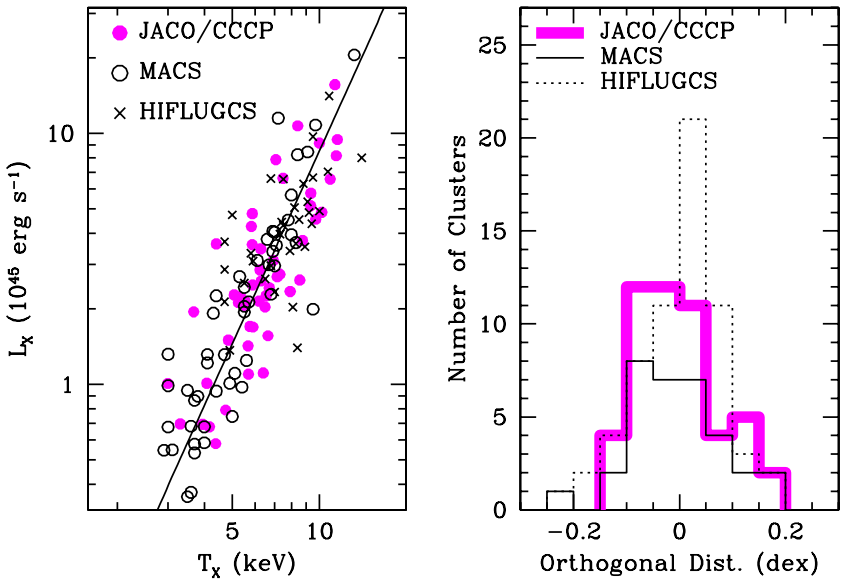

Figure 1. Comparison of the luminosity–temperature relationship for JACO/CCCP sample (solid dots), HIFLUGCS (open dots), and MACS (crosses).
(A color version of this figure is available in the online journal.)

such that r_Δ contains a mean matter density of Δ times the critical density of the universe at the redshift of the cluster) is a better choice, but even here, the value of Δ to use is not quite obvious. At the redshift of our sample, X-ray data quality tends to be best around r_{2500}, but most of the literature lists properties at r_{500}. Even after a choice of Δ, one must still decide whether to use the lensing or X-ray value, since they are not guaranteed to agree.

We choose to standardize the bulk of our discussion on the weak lensing overdensity radius $r_{500}^{\rm WL}$, because lensing masses are likely to be more unbiased for non-relaxed clusters (Meneghetti et al. 2010). For the most part, our results do not significantly change if we switch to X-ray r_{500}; one exception is the mass–temperature relation below, which tightens significantly with the switch. In Section 5.3, we also consider scaling relations with observables measured within fixed physical radii, because these are more likely to be useful for calibrating large data sets.

2.3. Weak Lensing Overview

The clusters in our sample were drawn from Hoekstra et al. (2012), which contains a weak lensing analysis of CFH12k and Megacam data from the CFHT. We refer interested readers to Hoekstra et al. (2012) for details of the data reduction and weak lensing analysis procedure.

We base our lensing masses on the aperture mass estimates (for details see the discussion in Section 3.5 in Hoekstra 2007). This approach has the advantage that it is practically model independent. Additionally, as the mass estimate relies only on shear measurements at large radii, contamination by cluster members is minimal. Hoekstra (2007) and Hoekstra et al. (2012) removed galaxies that lie on the cluster red-sequence and boosted the signal based on excess number counts of galaxies. As an extreme scenario we omitted those corrections and found that the lensing masses change by only a few percent; for details see Hoekstra et al. (2012). Hence our masses are robust against contamination by cluster members at the percent level.

The weak lensing signal, however, only provides a direct estimate of the *projected* mass. To calculate 3D masses from the model-independent 2D aperture masses we project and renormalize a density profile of the form $\rho_{\rm tot}(r) \propto r^{-1}(r_{200} + cr)^{-2}$ (Navarro et al. 1997). The relationship between the concentration c and the virial mass is fixed at $c \propto M_{200}^{-0.14}/(1+z)$ from numerical simulations (Duffy et al. 2008). Hence, the deprojection itself, though well motivated based on numerical simulations, is model dependent. However, the model dependence is weak—20% variations in the normalization of the mass–concentration relationship yield ≈5% variations in the measured masses (Hoekstra et al. 2012, Section 4.3). We also note that the lensing analysis differs from the X-ray analysis in that in the X-ray analysis, no mass–concentration relationship is assumed (i.e., the concentrations and masses are allowed to vary independently). We plan to address the effects of relaxing the lensing mass–concentration relation in a future paper.

2.4. X-Ray Data Reduction

We refer the reader to Mahdavi et al. (2007) for details of the X-ray data reduction procedure, which we briefly summarize and update here. We use both *Chandra* CALDB 4.2.2 (2010 April) and CALDB 4.4.7 (2011 December). We also check our results against the latest CALDB (4.5.1) at the time of writing. For *XMM-Newton* we use calibration files up-to-date to 2012 January; we also checked calibration files dating as far back as 2010 April. We detected no statistically significant changes in the calibration files over this period for either *Chandra* or *XMM-Newton*, except as detailed in Section 2.6 below.

We follow a standard data reduction procedure. We use the software packages CIAO (*Chandra*) and SAS (*XMM-Newton*) to process raw event files using the recommended settings for each observation mode and detector temperature. Where possible, we make event grade selections that maximize the data quality for extended sources (including the VFAINT mode optimizations for *Chandra*). We use the wavelet detection algorithm WAVDETECT on exposure-corrected images to identify contaminating sources; we masked out point and extended sources using the detected wavelet radius. Each masking was checked by eye for missing extended sources or underestimated masking radii.

The bulk of the X-ray background consists of a particle component which bypasses the mirror assembly, plus an astrophysical component that is folded through the mirror response. To remove the particle background we match the 8–12 keV photon count rate from the outer regions of each detector to the recommended blank sky observations for each detector, and then subtract the renormalized blank-sky spectra. What remains is the source plus an over- or undersubtracted astrophysical background, plus in some cases residual particle background. All these residual backgrounds are modeled jointly with the spatially resolved ICM model spectra, and their parameters marginalized over for the final results.

To extract spatially resolved spectra, we find the surface brightness peak in the *Chandra* image (if available) or *XMM-Newton* image (if *Chandra* is not available). We then draw circular annuli that contain a minimum of 1500 background-subtracted photon counts; where both *Chandra* and *XMM-Newton* data are available, the annuli are taken to be exactly the same for both sets of observations, with the minimum count requirement being imposed on the *Chandra* data (for photons within 8′) or *XMM-Newton* data (for photons outside 8′). We then compute appropriately weighted ancillary response files (ARF) and redistribution matrix files (RMF) for each spectrum, and subtract appropriately scaled particle background spectra. We emphasize that all spectra for each cluster undergo a simultaneous joint fit using a forward-convolved spectral model of the entire cluster, so that the choice of 1500 background-subtracted counts is not a sensitivity-limiting factor. That is to say, in no case is a single measurement derived from a single spectrum of 1500 counts, but rather such spectra are fit together in large batches on a cluster-by-cluster basis.

The detailed properties of the sample, including global X-ray temperatures and bolometric X-ray luminosities, masses, and substructure measures, are listed in Tables 1 and 2.

2.5. X-Ray Mass Modeling

Here we summarize and update the modeling procedure of Mahdavi et al. (2007), in which the cluster is spherically symmetric and the gas is in thermal pressure supported HSE within the cluster potential. The essence of the technique is to directly compare the observed spatially resolved spectra with model predictions. For a spectrum observed in an annulus with inner and outer radii R_1 and R_2, the model is

$$L_\nu = \int_{R_1}^{R_2} 2\pi R dR \int_R^{r_{\rm max}} n_e n_H \Lambda_\nu[T(r), Z(r)] \frac{2r dr}{\sqrt{r^2 - R^2}}, \quad (1)$$

where r denotes unprojected radius, R denotes projected radius, $r_{\rm max}$ is the termination radius of the X-ray gas (taken to be r_{100} in this paper), Λ_ν is the frequency-dependent cooling function which is a function of temperature T and metallicity Z, and n_e and n_H are the electron and hydrogen number density, respectively.

One feature of the above method is that the unprojected temperature profile is calculated self-consistently assuming HSE of assumed gas and dark matter density profiles. As a result, we never have to specify or fit a temperature profile; temperature is merely an intermediate "dummy" quantity connecting the gas and dark matter mass distributions to the X-ray spectra. This avoids subjective weighting involved in the fitting of 2D projected temperature profiles (Mazzotta et al. 2004; Rasia et al. 2005; Vikhlinin 2006), which are more difficult to correct for the effects of PSF distortion.

2.6. Parameters of the Hydrostatic Model

The hydrostatic model assumes a flexible spherical electron density distribution

$$n(r) = n_{e_0} \left(\frac{r}{r_{x_0}}\right)^{-\alpha} B(r, r_{x_0}, \beta_0) + n_{e_1} B(r, r_{x_1}, \beta_1) + n_{e_2} B(r, r_{x_2}, \beta_2), \quad (2)$$

where the familiar "beta" model is

$$B(r, r_{x_i}, \beta_i) = \left(1 + \frac{r}{r_{x_i}}\right)^{-\frac{3\beta_i}{2}}. \quad (3)$$

In other words, the gas mass profile consists of a fully general triple "beta" model profile, where the first beta model is further allowed to be multiplied by a single power law. The metallicity distribution is modeled as (e.g., Pizzolato et al. 2003)

$$\frac{Z}{Z_\odot} = Z_0 \left(1 + \frac{r^2}{r_z^2}\right)^{-3\beta_z} \quad (4)$$

with r_Z, β_z, and Z_0 free parameters. Finally, the total mass distribution (baryons and dark matter) is modeled as a Navarro et al. (1997) profile:

$$\rho_{\rm tot} = \frac{M_0}{r(cr + r_\Delta)^2}, \quad (5)$$

where M_0 is the normalization, c is the halo concentration, and r_Δ is the overdensity radius (see above). These are also free parameters, except that rather than fitting M_0, we fit M_Δ—the mass within r_Δ—as the normalization constant (because there is a one-to-one relationship between M_0 and M_Δ).

In general, some of the above parameters are better determined than the others. For example, the inner slope of the gas density distribution, α, is always well measured (with a typical uncertainty of ± 0.1, and follows the well-known trend (e.g., Sanderson & Ponman 2010) that low central entropy clusters have steeper inner profiles, $\alpha \approx 0.5$, whereas high entropy clusters have flatter profiles, $\alpha \approx 0$). The central metallicities are similarly well-determined. On the other hand, quantities such as the slopes and core radii of multiple β-model profiles—such as β_2 and β_3 or r_Z and β_Z—frequently reveal significant degeneracies with each other. In all cases, such degeneracies are properly marginalized over using the Hrothgar Markov Chain Monte Carlo procedure described in Mahdavi et al. (2007), and the one-dimensional error bars in Table 2 always properly reflect any and all degeneracies among the many parameters in this many-dimensional model.

2.7. Joint Calibration of Chandra and XMM-Newton Masses

Where available, we use both *Chandra* and *XMM-Newton* data for a cluster. This has several advantages: in the inner regions, *Chandra* is able to resolve the cluster cores well; while *XMM-Newton*'s wider field of view yields better coverage of the outer regions of the cluster. The simultaneous coverage of intermediate regions helps constrain residual backgrounds following blank sky subtraction.

When combining *Chandra* and *XMM-Newton* data, cross-calibration is a significant issue. In general, there are slight differences among the responses of the *Chandra* ACIS and the *XMM-Newton* pn, MOS1, and MOS2 detectors. Even after

Table 2
Mass and Substructure Properties at r_{500}

Cluster	$r_{500}^{\rm WL}$ (Mpc)	$M_{\rm WL}$ ($10^{14}\,M_\odot$)	$M_{\rm Gas}$ ($10^{14}\,M_\odot$)	$M_{\rm hydro}$ ($10^{14}\,M_\odot$)	K_0 (keV cm^2)	$D_{\rm BCG}$ (kpc)	w_X ($10^3 \times r_{500}^{\rm WL}$)	$P3/P0$ ($\times 10^{-7}$)
3C295	1.06 ± 0.06	5.7 ± 1.2	0.62 ± 0.03	3.9 ± 1.0	12.8 ± 2.4	12	5.7 ± 1.4	0.25 ± 0.20
A0068	1.16 ± 0.09	5.9 ± 1.6	0.77 ± 0.01	5.1 ± 1.0	214.2 ± 29.5	15	14.0 ± 2.1	0.74 ± 0.60
A0115N	1.03 ± 0.12	3.9 ± 1.5	0.60 ± 0.01	4.1 ± 0.2	30.0 ± 2.4	10	59.6 ± 0.8	3.31 ± 0.82
A0115S	1.14 ± 0.07	5.3 ± 1.2	0.80 ± 0.01	4.2 ± 0.3	192.8 ± 48.5	143	...	...
A0209	1.24 ± 0.07	6.8 ± 1.4	1.02 ± 0.02	5.6 ± 1.1	152.7 ± 20.9	16	7.1 ± 1.1	1.47 ± 1.10
A0222	1.16 ± 0.07	5.7 ± 1.3	0.61 ± 0.01	2.4 ± 0.6	220.2 ± 32.2	10	38.4 ± 3.2	1.21 ± 0.96
A0223S	1.24 ± 0.10	6.9 ± 2.0	0.68 ± 0.04	3.3 ± 1.6	133.5 ± 20.1	8	36.9 ± 2.4	2.26 ± 1.62
A0267	1.13 ± 0.09	5.3 ± 1.5	0.63 ± 0.01	5.7 ± 0.6	160.8 ± 20.6	77	22.0 ± 1.7	0.27 ± 0.22
A0370	1.43 ± 0.06	12.8 ± 2.0	1.00 ± 0.05	8.6 ± 6.0	500.1 ± 159.8	23	15.8 ± 1.3	0.62 ± 0.49
A0383	1.04 ± 0.13	4.0 ± 1.8	0.39 ± 0.01	4.6 ± 0.6	21.3 ± 1.0	<3	3.1 ± 0.6	0.36 ± 0.26
A0520	1.16 ± 0.07	5.6 ± 1.3	0.85 ± 0.01	7.3 ± 0.3	590.1 ± 39.4	341	100.7 ± 0.7	4.66 ± 0.97
A0521	1.19 ± 0.08	6.3 ± 1.6	1.06 ± 0.02	5.0 ± 1.3	75.6 ± 18.1	33	58.5 ± 1.7	8.59 ± 3.41
A0586	1.18 ± 0.09	5.6 ± 1.6	0.65 ± 0.08	3.9 ± 0.6	140.1 ± 23.5	11	7.3 ± 1.6	0.59 ± 0.49
A0611	1.13 ± 0.06	5.7 ± 1.3	0.66 ± 0.05	6.0 ± 0.9	57.0 ± 9.0	4	8.0 ± 0.8	0.68 ± 0.42
A0697	1.35 ± 0.05	9.7 ± 1.3	1.56 ± 0.03	10.9 ± 1.5	240.0 ± 45.4	20	9.1 ± 1.1	0.20 ± 0.16
A0851	1.32 ± 0.09	10.5 ± 2.5	0.97 ± 0.02	7.4 ± 2.3	479.7 ± 79.7	278	30.5 ± 3.4	13.15 ± 7.51
A0959	1.26 ± 0.07	7.8 ± 1.7	0.75 ± 0.03	5.6 ± 0.5	203.8 ± 23.7	36	42.6 ± 4.5	7.70 ± 6.55
A0963	1.00 ± 0.10	3.7 ± 1.3	0.57 ± 0.01	4.7 ± 0.5	63.1 ± 5.9	6	5.5 ± 0.5	0.12 ± 0.10
A1689	1.57 ± 0.09	13.7 ± 2.7	1.27 ± 0.01	9.7 ± 0.6	72.5 ± 5.5	5	4.1 ± 0.3	0.08 ± 0.04
A1758E	1.37 ± 0.08	10.1 ± 2.3	1.23 ± 0.04	9.4 ± 0.6	227.4 ± 28.5	25	117.9 ± 1.2	8.42 ± 1.62
A1758W	1.37 ± 0.06	10.0 ± 1.4	0.93 ± 0.07	11.5 ± 1.6	194.5 ± 19.9	25	117.9 ± 1.2	8.42 ± 1.62
A1763	1.40 ± 0.10	10.1 ± 2.5	1.34 ± 0.01	3.9 ± 0.7	419.5 ± 54.0	7	22.9 ± 1.2	0.97 ± 0.64
A1835	1.30 ± 0.05	8.4 ± 1.3	1.21 ± 0.01	9.9 ± 0.7	19.7 ± 0.4	6	3.9 ± 0.2	<0.1
A1914	1.18 ± 0.05	5.6 ± 1.0	0.99 ± 0.00	9.2 ± 0.9	128.7 ± 9.5	86	27.8 ± 0.5	2.39 ± 0.40
A1942	1.05 ± 0.06	4.3 ± 1.0	0.44 ± 0.01	2.7 ± 0.6	230.6 ± 72.2	4	9.3 ± 1.4	1.57 ± 1.21
A2104	1.22 ± 0.08	6.1 ± 1.6	0.68 ± 0.14	5.8 ± 0.8	201.7 ± 44.2	8	...	...
A2111	1.07 ± 0.10	4.5 ± 1.5	0.74 ± 0.07	7.3 ± 2.5	203.8 ± 55.6	129	33.0 ± 2.8	3.22 ± 2.43
A2163	1.38 ± 0.11	9.5 ± 2.5	2.33 ± 0.03	12.0 ± 1.2	336.0 ± 18.0	160	35.3 ± 0.4	3.76 ± 0.37
A2204	1.34 ± 0.07	8.1 ± 1.6	1.16 ± 0.01	8.7 ± 0.6	17.3 ± 0.3	<3	4.8 ± 0.3	<0.1
A2218	1.14 ± 0.08	5.1 ± 1.4	0.72 ± 0.01	4.3 ± 0.6	317.9 ± 44.9	60	18.9 ± 1.0	1.28 ± 0.53
A2219	1.35 ± 0.07	9.1 ± 1.9	1.65 ± 0.03	7.1 ± 0.9	243.2 ± 33.3	8	...	...
A2259	1.05 ± 0.09	4.0 ± 1.2	0.50 ± 0.04	4.1 ± 0.9	134.7 ± 30.1	78	24.1 ± 1.7	1.18 ± 0.95
A2261	1.52 ± 0.05	12.9 ± 1.6	1.46 ± 0.13	6.6 ± 1.0	60.0 ± 9.0	<2	14.3 ± 1.0	0.39 ± 0.21
A2390	1.33 ± 0.06	8.6 ± 1.5	1.48 ± 0.01	11.0 ± 0.9	31.6 ± 1.1	4	11.1 ± 0.9	1.24 ± 0.17
A2537	1.22 ± 0.05	7.2 ± 1.1	0.86 ± 0.06	5.9 ± 0.9	91.8 ± 21.7	17	8.4 ± 1.3	0.99 ± 0.74
CL0024.0+1652	1.30 ± 0.10	9.8 ± 2.7	0.45 ± 0.08	3.1 ± 4.7	61.2 ± 15.9	24	73.5 ± 11.5	6.46 ± 5.23
MACSJ0717.5+3745	1.46 ± 0.07	16.6 ± 3.4	2.35 ± 0.03	12.3 ± 1.9	396.3 ± 80.0	224	23.9 ± 0.9	23.09 ± 3.24
MACSJ0913.7+4056	0.95 ± 0.07	4.0 ± 1.3	0.53 ± 0.02	4.8 ± 0.7	17.0 ± 1.1	4	4.3 ± 1.0	0.40 ± 0.19
MS0015.9+1609	1.60 ± 0.06	21.9 ± 3.2	2.01 ± 0.06	13.4 ± 1.9	171.0 ± 20.0	41	8.6 ± 1.1	0.58 ± 0.38
MS0440.5+0204	0.85 ± 0.06	2.2 ± 0.7	0.24 ± 0.05	2.8 ± 0.5	30.1 ± 5.7	<3	19.6 ± 4.2	1.38 ± 1.16
MS0451.6−0305	0.95 ± 0.10	4.5 ± 1.7	1.03 ± 0.02	7.8 ± 1.0	235.3 ± 43.3	28	11.9 ± 1.1	1.44 ± 0.82
MS0906.5+1110	1.36 ± 0.09	8.7 ± 1.9	0.87 ± 0.03	3.5 ± 0.5	148.9 ± 29.0	3	17.1 ± 1.2	0.20 ± 0.14
MS1008.1−1224	1.06 ± 0.05	4.8 ± 0.9	0.58 ± 0.04	7.3 ± 3.1	97.9 ± 24.7	10	55.8 ± 2.2	4.17 ± 2.33
MS1231.3+1542	0.54 ± 0.11	0.6 ± 0.4	0.14 ± 0.00	1.4 ± 0.1	131.5 ± 16.5	72	6.9 ± 1.4	5.08 ± 3.82
MS1358.1+6245	1.12 ± 0.09	5.9 ± 1.6	0.67 ± 0.07	7.6 ± 0.9	39.3 ± 3.9	4	8.6 ± 1.2	0.34 ± 0.29
MS1455.0+2232	1.04 ± 0.05	4.2 ± 0.8	0.56 ± 0.01	3.1 ± 0.2	23.6 ± 0.8	3	4.9 ± 0.2	0.13 ± 0.06
MS1512.4+3647	0.85 ± 0.18	2.6 ± 1.8	0.34 ± 0.03	2.1 ± 0.7	26.4 ± 8.1	6	6.7 ± 1.3	1.30 ± 1.09
MS1621.5+2640	1.19 ± 0.07	7.7 ± 1.8	0.83 ± 0.03	5.4 ± 0.8	182.1 ± 37.7	41	19.0 ± 4.3	7.47 ± 5.43
RXJ1347.5−1145	1.25 ± 0.12	9.3 ± 2.9	1.63 ± 0.01	13.1 ± 1.8	29.7 ± 2.1	<4	12.6 ± 1.4	1.30 ± 0.41
RXJ1524.6+0957	0.87 ± 0.12	3.4 ± 1.8	0.41 ± 0.04	2.7 ± 0.4	123.9 ± 42.3	22	63.2 ± 5.6	22.92 ± 15.12

Notes. All quantities are measured at $r_{500}^{\rm WL}$, except for $P3/P0$ power ratio, which is measured at $r_{2500}^{\rm WL}$, and $D_{\rm BCG}$, which is in Mpc. $M_{\rm X}$ is the X-ray hydrostatic mass, K_0 is the entropy at 20 kpc, $w_{\rm BCG}$ is the X-ray peak to BCG offset, w_X is the centroid shift. Lensing masses are from Hoekstra et al. (2012).

over a decade in flight, the source of these differences has not been conclusively identified. Typically, comparisons show that *Chandra* temperatures are 5%–15% higher (Snowden et al. 2008; Reese et al. 2010). The most recent calibration tests (Tsujimoto et al. 2011) use the G21.5-0.9 pulsar (which is fainter than the usual source, the Crab nebula, and hence not subject to detector pileup). Tsujimoto et al. (2011) find that the *XMM-Newton* pn has a 15% lower flux in the 2.0–8.0 keV energy band compared to the *Chandra* ACIS-S. This confirms an earlier finding by Nevalainen et al. (2010) who found similar results. Lower hard band flux naturally leads to lower X-ray temperatures when 0.5–2.0 keV photons are also included. This primarily affects masses for which spectral line emission is not dominant (i.e., in hot, $kT > 4$ keV clusters). It is at this point unknown where the source of the disagreement lies and which instrument is better calibrated.

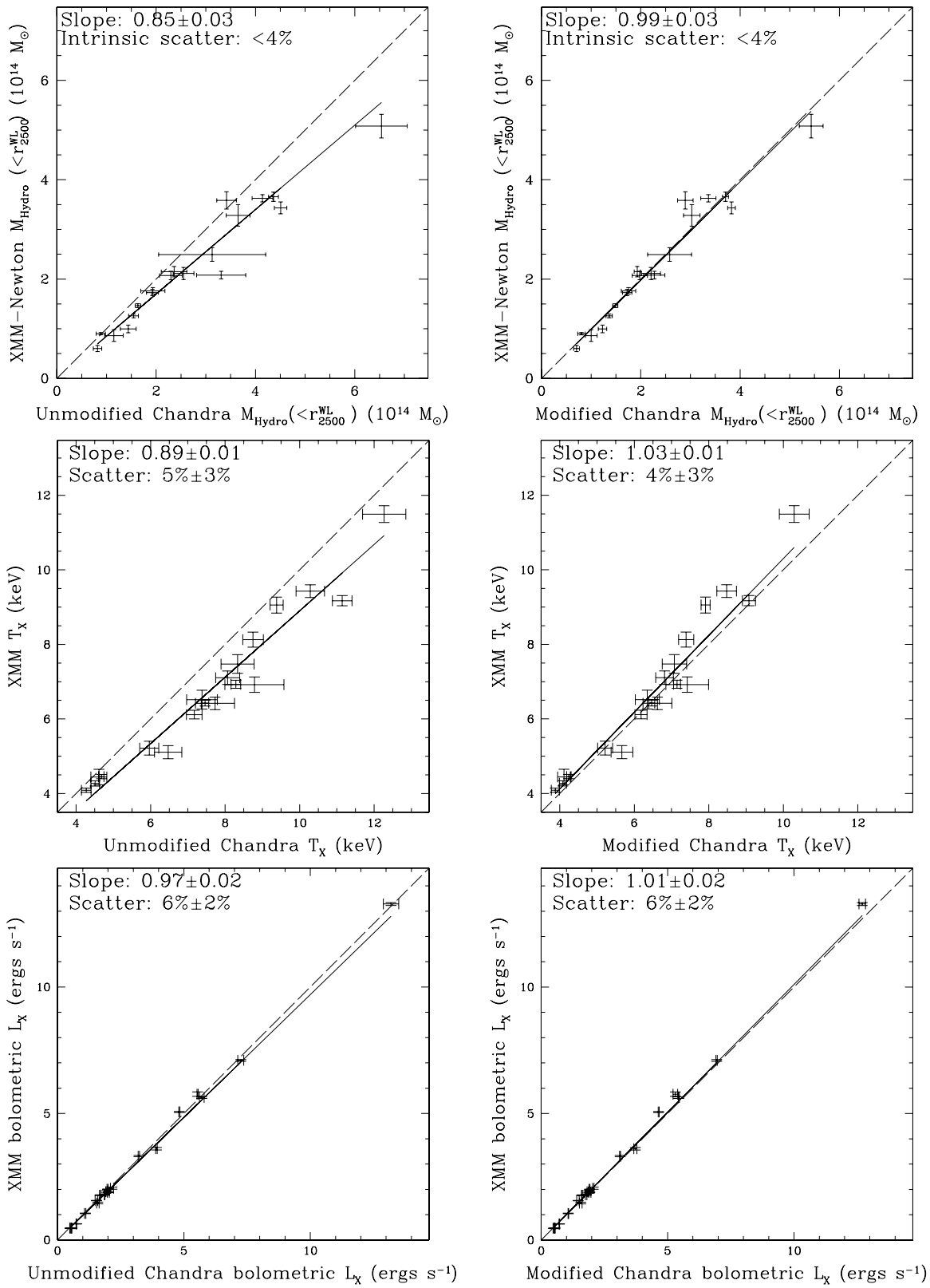

Figure 2. Comparison of *XMM-Newton* and *Chandra* X-ray masses (top), temperatures (middle), and bolometric X-ray luminosities (bottom) within lensing r^{WL}_{2500}. The left-hand column shows the unmodified *Chandra* values, while the right-hand column shows the result of scaling the *Chandra* effective area by a power law in energy of slope $\zeta = 0.07$, *Chandra* and *XMM-Newton* observables come into better agreement. The dashed line shows equality in all cases.

Figure 2 shows the X-ray mass measured within lensing r^{WL}_{2500} for the 19 clusters in our sample which contain both *Chandra* and *XMM-Newton* data. Shown are the results for CALDB 4.2.2 (2010 April). We also checked CALDB 4.4.7 (2011 December) and CALDB 4.5.1 (2012 June). The calibration for our sample changed little during this period, and in all three cases, we find that *Chandra* masses are higher than *XMM-Newton* masses by roughly 15%. All observations were recorded prior to 2010, and

taken as a whole, the change in the *Chandra* masses of these systems is not statistically significant between CALDB 4.2.2 and 4.4.7. We adopt the 2010 CALDB for the remainder of this paper, stressing that any changes to our results would be well within the statistical errors presented were we to switch to a different calibration release.

To be able to combine *Chandra* and *XMM-Newton* data, one must first ensure that they are consistent. We find that the following simple cross-calibration prescription is able to bring the data into self-consistency:

$$A_{\rm CXO}^{\rm corrected}(E) = A_{\rm CXO}(E)\left(\frac{E}{\rm keV}\right)^{\zeta}, \quad (6)$$

where $\zeta = 0$ gives the unmodified CALDB area, and $\zeta > 0$ has the effect of down-weighting the high-energy effective area of *Chandra*. We find that setting $\zeta = 0.07$ brings *Chandra* and *XMM-Newton* masses into agreement as shown in Figure 2. In either case, the intrinsic scatter between *Chandra* and *XMM-Newton* mass measurements at these fixed radii is certainly less than 10%, though inconsistent with zero at the 2σ level.

Figure 2 also shows that the integrated X-ray temperatures and luminosities within lensing r_{2500} are also improved by our suggested calibration. The discrepancy between unmodified *Chandra* X-ray temperatures and *XMM-Newton* temperatures is roughly the same as the discrepancy in hydrostatic masses. The bolometric X-ray luminosities are also in better agreement as a result of the effective area re-calibration, though in this case the original discrepancy is less severe than in the realm of the spectroscopic temperature.

We chose to modify the *Chandra* effective area, and not the *XMM-Newton* effective area, based on the fact that *XMM-Newton* has exhibited the least variation over the years, whereas *Chandra* has enacted larger 10%–15% changes in its effective area calibration historically. We note that had we modified the *XMM-Newton* effective area to match that of *Chandra*, then we would have found in what follows that clusters no longer exhibit self-similar behavior and that (1) those with obvious substructure would be the ones whose masses calculated assuming HSE would agree with their weak lensing masses, and (2) that clusters with cool cores would have hydrostatic masses greater than their weak lensing masses. This uncertainty in the telescopes' effective areas must be viewed as a fundamental systematic limitation of X-ray astronomy at least as related to cluster science.

2.8. Online Data and Regression Tool

All data and analysis software used for this paper are available online at http://sfstar.sfsu.edu/cccp. Fits of scaling relations (i.e., the modeling of linear or power law relationships among measured quantities) are complicated by the fact that error in both coordinates makes ordinary χ^2 analysis invalid. A detailed treatise of recent developments in the theory behind modeling 2D data with errors in both coordinates appears in Hogg et al. (2010). These techniques allow the simultaneous estimation of slope, intercept, and intrinsic scatter in such relations. We implement the methods of Hogg et al. (2010) at the data Web site for this article.

3. MEASURES OF NON-RELAXED STATUS

The gas in all clusters of galaxies exhibits some degree of deviation from an idealized smooth, triaxial distribution. Such deviation could come in terms of subclumping, asymmetry, or both. Its presence gives some clue as to the nature of its evolutionary history; for example, asymmetry could indicate either the beginning or the end of a merger event; subclumps could either be recently accreted small groups of galaxies, or surviving cold cores from recent mergers.

Despite this ambiguity, objective measures of substructure are helpful in arriving at quantitative estimates of departure from equilibrium. To begin, we employ two common and well-tested measures of substructure: power ratios and centroid shift variance. Power ratios are Fourier-space estimators of fluctuations in the overall cluster surface brightness distribution, while the centroid shift is a measure of the variance of the distance between the X-ray surface brightness peak (which is always well defined) and the centroid (which in a non-relaxed cluster often varies significantly as a function isophote used for its estimation). We refer the reader to Buote & Tsai (1995), Poole et al. (2006), Jeltema et al. (2005), Jeltema et al. (2008), and Böhringer et al. (2010) for details on the calculation of these estimators.

As further tracers of the relaxed or non-relaxed state of a system, we also consider the somewhat more straightforward measures, central entropy and the X-ray to optical center offset. Low central entropies indicate the presence of a cool core, which tend to be associated (non-exclusively) with relaxed clusters. We define the central entropy as

$$K_0 \equiv K(20\,{\rm kpc}). \quad (7)$$

In other words, the central entropy is defined as the deprojected entropy profile evaluated at a radius of 20 kpc from the cluster center.

Similarly, the distance between the brightest cluster galaxy (BCG) and the X-ray surface brightness peak can be a good predictor of relaxed state, with large shifts indicating ongoing or residual merger activity (Poole et al. 2007). We measure this distance via simple astrometry on X-ray and optical images, and call it $D_{\rm BCG}$.

One would expect relaxed halos to be more representative of idealized halo growth models. Hence we expect scaling relations among the various thermodynamic and dark matter parameters to be tighter for clusters selected on the basis of the more well-behaved substructure indicators. We also expect the most powerful substructure measures to be correlated with each other.

3.1. Correlations among Measures of Substructure

We explore the possibility of whether our substructure measures show inherent correlation. The presence of such correlations, particularly when involving both X-ray and optical data, can serve as road maps toward our goal of quantifying departures from equilibrium as economically as possible. We use the Spearman's rank correlation coefficient, with bootstrap resampling for determining 1σ uncertainties.

The relationship between central entropy and BCG offset is the most significant correlation in our sample. This also happens to be the most interesting correlation due to the relative ease of deriving central entropy and BCG offset from observables. Figure 3 shows that the two substructure measures appear to form a two-peaked joint distribution, with low central entropy, low BCG offsets in one corner, and high central entropy, high BCG offset clusters in another. The dividing line is best seen as

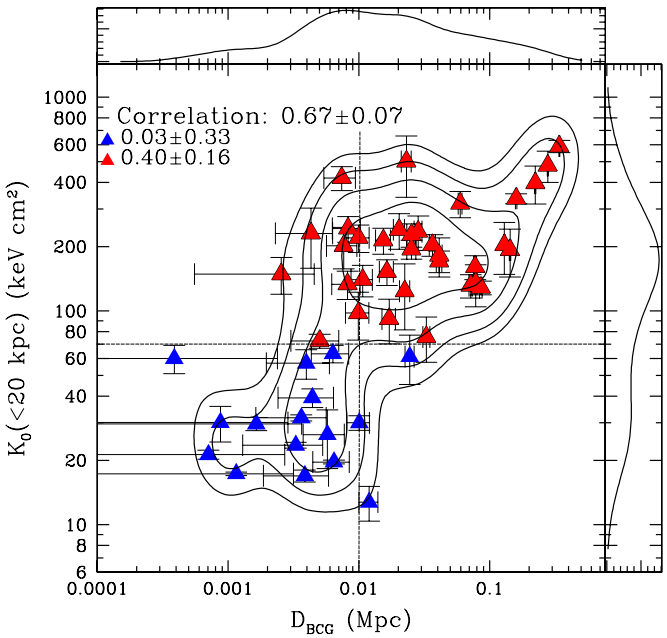

Figure 3. Bimodality in the joint distribution of BCG offset and central entropy; contours show lines of constant probability density after the points have been smoothed with a 0.25 dex Gaussian. The top and right axes show the 1D probability density for central entropy and BCG offset. Blue triangles show cool-core clusters and red triangles show non-cool-core clusters. The horizontal thin line shows our chosen division between cool-core and non-cool-core systems, while the vertical line shows our chosen division between low BCG offset and high BCG offset systems.

(A color version of this figure is available in the online journal.)

a curve with equation

$$K_0 = 7\,\mathrm{keV\,cm^2}\left(\frac{D_{\mathrm{BCG}}}{\mathrm{Mpc}}\right)^{-1/2}. \quad (8)$$

The high correlation coefficient between K_0 and D_{BCG} appears to be due to bimodality: when we calculate the correlation coefficient separately for either cloud, we find that the clouds individually do not contain significant internal correlation. Though the above formula offers the most clean separation between the two clouds, most of the separation can be captured by imposing cuts in entropy, or, somewhat less cleanly, in BCG offset.

For this reason, throughout the rest of the paper, we introduce a labeling system that represents cuts in these two most easily measured substructure estimators. We use blue triangles to indicate $K_0 < 70$ keV cm^2 ("cool core systems" or CC), and red triangles to indicate $K_0 > 70$ keV cm^2 ("non-cool-core systems" or NCC). This nomenclature is based on the fact that 70 keV cm^2 corresponds to a cooling time of ≈1.5 Gyr; most cool-core clusters have central cooling times below this value.

Similarly, we use blue circles to indicate systems with $D_{\mathrm{BCG}} < 0.01$ Mpc ("low BCG offset systems") and red circles to indicate $D_{\mathrm{BCG}} > 0.01$ Mpc ("high BCG offset systems").

In Figure 4, we look for inherent correlations among the other various indicators of substructure. Strong correlations exist between the BCG offset D_{BCG}, the central entropy K_0, the X-ray centroid shift w_X at r_{500}^{WL}, and the $P3/P0$ ratio at r_{2500}^{WL} (in measuring the latter two, we cut out the central 0.15 r_{500}^{WL} to avoid dilution of the signal by the cool core). Interestingly, the $P3/P0$ ratio measured at r_{500}^{WL} (instead of r_{2500}^{WL}) showed much larger scatter (presumably due to noise) and proved much less tightly correlated with the other substructure measures than the $P3/P0$ ratio at r_{2500}^{WL}.

In particular, it should be noted that $P3/P0$ exhibits almost as strong a correlation with BCG offset as does central entropy, though there is no evidence for bimodality. For non-cool-core clusters, the $P3/P0$ is *significantly more* correlated with BCG offset than is the central entropy. This is quite a surprising result, since $P3/P0$ traces cluster dynamics outside the cool core, whereas the central entropy is more sensitive to the inner parts.

The BCG correlation trends are consistent with the well-known tendency of cool cores to occur in smoother (i.e., more relaxed, hence lower w_X, low power ratio) clusters where a BCG sits close to the bottom of the potential well (Bildfell et al. 2008). This demonstrates the tight quantitative link between these completely independent X-ray and optical indicators of substructure.

4. THE L_X–T_X RELATION

Similarly to previous studies (e.g., Morandi et al. 2007; Pratt et al. 2010; Mittal et al. 2011), we find that the luminosity–temperature (L_X–T_X) relationship exhibits a significant scatter of ≈50% when the core of the cluster is included—a scatter which is diminished considerably, to 36%, when the core is excised. This effect is due to the overall non-self-similarity of cluster cool cores in comparison to the regions outside the cool core (e.g., Vikhlinin et al. 2006). When the core is not excised, the cool-core clusters lie significantly above the non-cool-core clusters, an effect first noted by Fabian et al. (1994) and subsequently studied in detail by McCarthy et al. (2004) and Maughan et al. (2012).

In Figure 5 and Table 3, we show that when we include all cluster emission, the residuals of the L_X–T_X relation show a strong and significant correlation with both the central entropy of the cluster and the centroid shift w_X (we choose w_X because of the four measures discussed in Section 3.1 it offers the strongest correlation). However, when we cut out the central 0.15 r_{500}^{WL}, the distinction disappears, and the cool-core and non-cool-core clusters become indistinguishable in terms of entropy as well as w_X. This is consistent with the findings of Maughan et al. (2012) in the sense that once the cool core is taken out of consideration, residuals in the L–T relation no longer carry information regarding the dynamical state of the cluster.

This is an example of "irreversible scatter"—in other words, outside their cores, the clusters of galaxies in our sample have "forgotten" the cause of the intrinsic scatter in the L_X–T_X relation. This has implications for scaling relation correction procedures such as described in, e.g., Jeltema et al. (2008), where relationships between the residuals and the substructure measures for simulated clusters are used to produce corrected observables which sit more tightly on the scaling relations. The lack of correlation in our case implies that such procedures will not reduce the scatter in the measured scaling relations (at least for the JACO/CCCP sample).

5. LENSING MASS–OBSERVABLE RELATION

The mass–observable relationship is an important ingredient in the determination of the cosmological parameters with clusters of galaxies. Because the mass function is the ultimate connector between the cosmological parameters and the data, finding accurate mass proxies using multiple methods and wavelength regimes is important. Comparison of X-ray derived

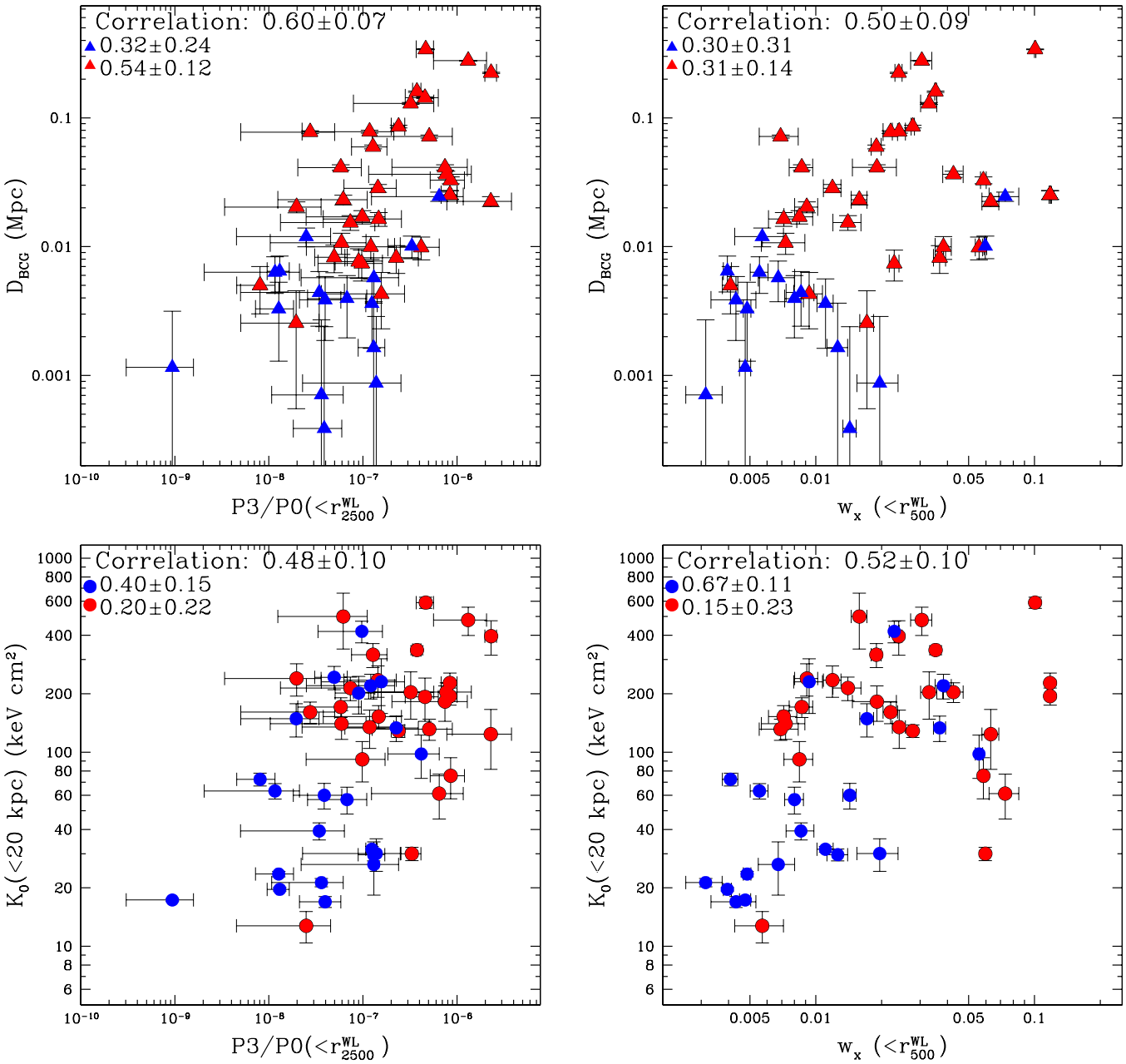

Figure 4. Correlation of four different substructure measures (central entropy K_0, BCG offset $D_{\rm BCG}$, X-ray centroid variance w_X, and $P3/P0$ power ratio) against each other. Blue triangles show cool-core clusters and red triangles show non-cool-core clusters; blue circles show low BCG offset systems and red circles show high BCG offset systems.

(A color version of this figure is available in the online journal.)

observables with weak gravitational lensing masses, which do not require the assumption of HSE, has proved a fruitful path toward this end (e.g., Mahdavi et al. 2008; Okabe et al. 2010; Jee et al. 2011). We list our results for several different mass–observable relations in Table 3.

5.1. Temperature, Gas Mass, and Pseudo-Pressure

We begin by examining the lensing mass–gas temperature relationship in Figure 6; while exhibiting significant intrinsic scatter (Ventimiglia et al. 2008; Zhang et al. 2008; Mantz et al. 2010), the *M–T* relation is still a worthwhile keystone for comparison with previous work. We find that the relationship is consistent with being self-similar, with a larger scatter and uncertainty at lensing r_{500} than at X-ray r_{500}. Regardless of whether we consider the cool-core or the non-cool-core subsamples, the scatter is roughly 46%. The scatter drops dramatically to 17%±8% when we use X-ray r_{500} because of the inherent correlation between the gas temperature and X-ray r_{500} itself, which we do not attempt to model. The phenomenon of inherent correlation is discussed in greater detail by Kravtsov & Borgani (2012), and arises because the *aperture* used to measure the mass is highly correlated with the observable on the other axis (in this case, X-ray r_{500} and X-ray temperature are highly correlated).

The normalization derived for the mass–temperature relation is consistent with previous work, for example, Pedersen & Dahle (2007), Henry et al. (2009), and Okabe et al. (2010).

Table 3 also shows similar results for the core-excised X-ray luminosity–lensing mass (L_X–$M_{\rm WL}$) relation. The intrinsic scatter (35%±13%) is consistent with that of the mass–temperature

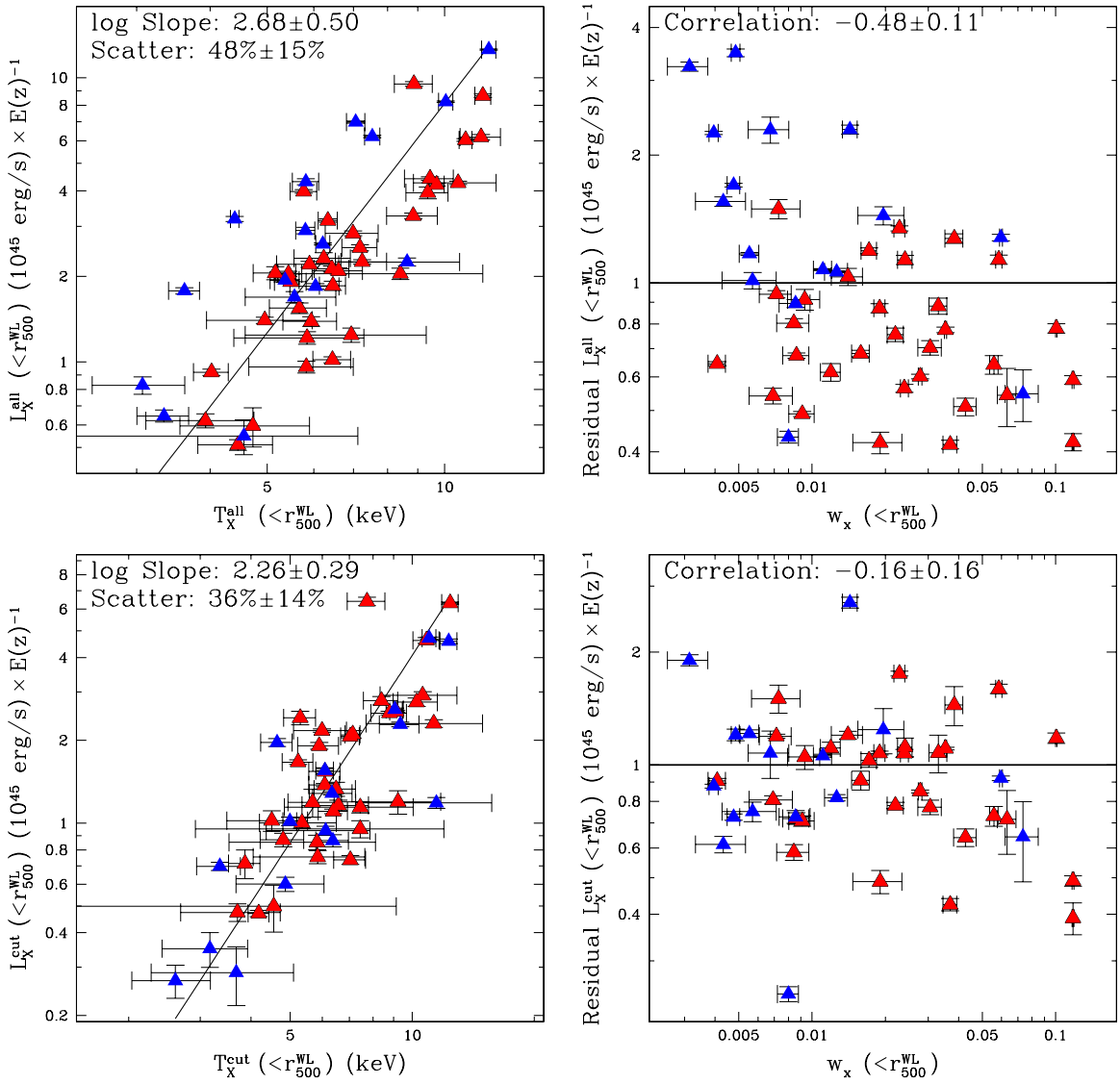

Figure 5. Top panels: the luminosity–temperature relationship at lensing $r_{500}^{\rm WL}$ and its residuals compared to centroid shift variance w_X. Bottom panels: same as top, except that the inner 0.15 $r_{500}^{\rm WL}$ has been removed. The residuals are uncorrelated with all four substructure measures. Blue triangles show cool-core clusters and red triangles show non-cool-core clusters.

(A color version of this figure is available in the online journal.)

relation, and as before, the scatter is dramatically lower at r_{500}^{X} than at $r_{500}^{\rm WL}$, again likely due to internal correlation between r_{500}^{X} and L_X, which we do not model.

Far more impressive is the gas mass–lensing mass relationship. The gas mass has been shown in previous work to be a useful mass proxy (Mantz et al. 2010; Okabe et al. 2010)—essentially, the assumption that rich clusters of galaxies have the same gas fraction is turning out to be a remarkably robust one. We improve the significance of the Okabe et al. (2010) finding with our sample of 50 clusters: at $r_{500}^{\rm WL}$, the gas mass is consistent with being proportional to the lensing mass, with a log slope of 1.04 ± 0.1, and a normalization implying a gas fraction $f_{\rm gas} = 0.12 \pm 0.01$.

We find a low scatter of $15\% \pm 8\%$ for the $M_{\rm gas}$–M_L relation (Figure 7) for all clusters, regardless of dynamical state. Interestingly, the same scatter holds regardless of whether we use lensing $r_{500}^{\rm WL}$ or a fixed aperture of 1 Mpc.

This low scatter at fixed radius is important. Recently, sophisticated treatments of the covariance between the axes in the mass–observable relation have become possible (Hogg et al. 2010). Specifically, in the case of gas mass and lensing mass measured at $r_{500}^{\rm WL}$, there is a subtle correlation between the two axes, even though one quantity (lensing mass) is measured using optical data and the other quantity (gas mass) is measured using X-ray data. The issue is that the aperture itself, $r_{500}^{\rm WL}$, depends on the lensing mass, and therefore, by choosing the same aperture for the gas mass, we might introduce a correlation that produces artificially low scatter. This effect was described in detail by Becker & Kravtsov (2011) who find that such correlations can result in the measured scatter being ≈50% smaller than the true scatter.

However, using a physical aperture of 1 Mpc completely takes away any possibility of covariance between the two axes. In Figure 8, we truly have two statistically independent observations, and yet the intrinsic scatter remains remarkably low, $16\% \pm 7\%$. The fact that the scatter does not change when switching to a fixed physical aperture is reassuring. The 1σ scatter uncertainties are just large enough to accommodate the

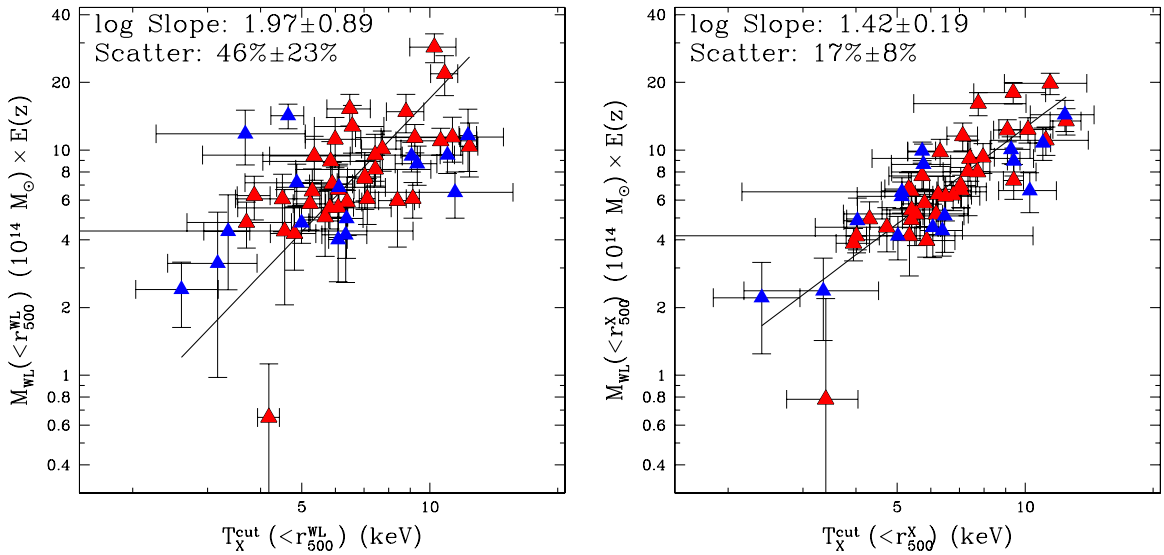

Figure 6. The mass–temperature relationship at lensing r_{500} (left) and at X-ray r_{500} (right). The latter shows less scatter due to the intrinsic correlation of X-ray r_{500} with temperature. Blue triangles show cool-core clusters and red triangles show non-cool-core clusters.

(A color version of this figure is available in the online journal.)

Table 3
Mass Proxy Fits with Lognormal Intrinsic Scatter

Proxy	Proxy Aperture	$M_{\rm WL}$ Aperture	Sample	Log Slope	Log Intercept	Fractional Scatter in $M_{\rm WL}$ at Fixed Proxy
			Relations at Fixed Overdensity in Proxy and Mass			
$T_X^{\rm cut}/8$ keV	$r_{500}^{\rm WL}$	$r_{500}^{\rm WL}$	All	1.97 ± 0.89	1.04 ± 0.06	0.46 ± 0.23
$T_X^{\rm cut}/8$ keV	r_{500}^{X}	r_{500}^{X}	All	1.42 ± 0.19	0.96 ± 0.02	0.17 ± 0.08
$L_X^{\rm cut} E(z)^{-1}$	$r_{500}^{\rm WL}$	$r_{500}^{\rm WL}$	All	0.54 ± 0.12	0.81 ± 0.04	0.36 ± 0.12
$L_X^{\rm cut} E(z)^{-1}$	r_{500}^{X}	r_{500}^{X}	All	0.57 ± 0.08	0.78 ± 0.03	0.27 ± 0.05
$M_{\rm Gas} E(z)$	$r_{500}^{\rm WL}$	$r_{500}^{\rm WL}$	All	1.04 ± 0.10	0.90 ± 0.02	0.15 ± 0.06
			$K_0 < 70$ keV cm^2	0.91 ± 0.20	0.89 ± 0.03	<0.1
			$K_0 > 70$ keV cm^2	1.09 ± 0.13	0.90 ± 0.02	0.18 ± 0.09
			$D_{\rm BCG} < 0.01$ Mpc	0.93 ± 0.13	0.89 ± 0.02	<0.06
			$D_{\rm BCG} > 0.01$ Mpc	1.13 ± 0.18	0.90 ± 0.03	0.22 ± 0.15
$Y_X E(z)^{0.6}$	$r_{500}^{\rm WL}$	$r_{500}^{\rm WL}$	All	0.56 ± 0.07	0.45 ± 0.07	0.22 ± 0.05
			$K_0 < 70$ keV cm^2	0.44 ± 0.14	0.53 ± 0.11	0.24 ± 0.18
			$K_0 > 70$ keV cm^2	0.62 ± 0.10	0.41 ± 0.09	0.21 ± 0.09
			$D_{\rm BCG} < 0.01$ Mpc	0.48 ± 0.09	0.52 ± 0.08	0.17 ± 0.11
			$D_{\rm BCG} > 0.01$ Mpc	0.65 ± 0.14	0.36 ± 0.13	0.27 ± 0.17
			Relations at Other Radii			
$T_X^{\rm cut}/8$ keV (keV)	1 Mpc	1 Mpc	All	1.10 ± 0.57	0.80 ± 0.02	0.15 ± 0.11
$L_X^{\rm cut}$	"	"	All	0.26 ± 0.07	0.71 ± 0.02	0.19 ± 0.04
$M_{\rm Gas}$	"	"	All	0.83 ± 0.14	0.90 ± 0.03	0.16 ± 0.10
Y_X	"	"	All	0.40 ± 0.06	0.48 ± 0.05	0.12 ± 0.04
$T_X^{\rm cut}/8$ keV	"	$r_{500}^{\rm WL}$	All	3.04 ± 1.38	1.03 ± 0.08	0.46 ± 0.31
$L_X^{\rm cut}$	"	$r_{500}^{\rm WL}$	All	0.58 ± 0.15	0.80 ± 0.04	0.38 ± 0.13
$M_{\rm Gas}$	"	$r_{500}^{\rm WL}$	All	1.73 ± 0.59	1.20 ± 0.13	0.39 ± 0.18
Y_X	"	$r_{500}^{\rm WL}$	All	0.80 ± 0.15	0.35 ± 0.11	0.28 ± 0.14

Notes. All proxies are fit against $M_{\rm WL} E(z)$ at an aperture of $r_{500}^{\rm WL}$ or $M_{\rm WL}$ at an aperture of 1 Mpc. All masses are in units of $10^{14}\ M_\odot$. The core-cut X-ray luminosity is in units of 10^{45} erg s^{-1}, and Y_X is in units of $10^{14}\ M_\odot$ keV. The self-similar evolution model for clusters of galaxies (e.g., Kaiser 1991; Kravtsov & Borgani 2012) posits $ME(z) \propto T_X^{3/2} \propto L_X^{3/4} E(z)^{-1} \propto Y_X^{3/5} E(z)^{3/5}$, where $E(z)^2 = \Omega_M (1+z)^3 + \Omega_\Lambda$.

scatter underestimate predicted by Becker & Kravtsov (2011) (e.g., if the "true" scatter at both $r_{500}^{\rm WL}$ and 1 Mpc is 20%, our 1σ errors would be consistent with a 50% scatter underestimate at $r_{500}^{\rm WL}$ and no scatter underestimate at 1 Mpc). In Table 3 we also list the performance of Y_X, L_X, and T_X, measured at fixed physical radius of 1 Mpc, as predictors of $M_{\rm WL}(<1\,{\rm Mpc})$. Overall, we find little difference between the intrinsic scatter at 1 Mpc compared to $r_{500}^{\rm WL}$.

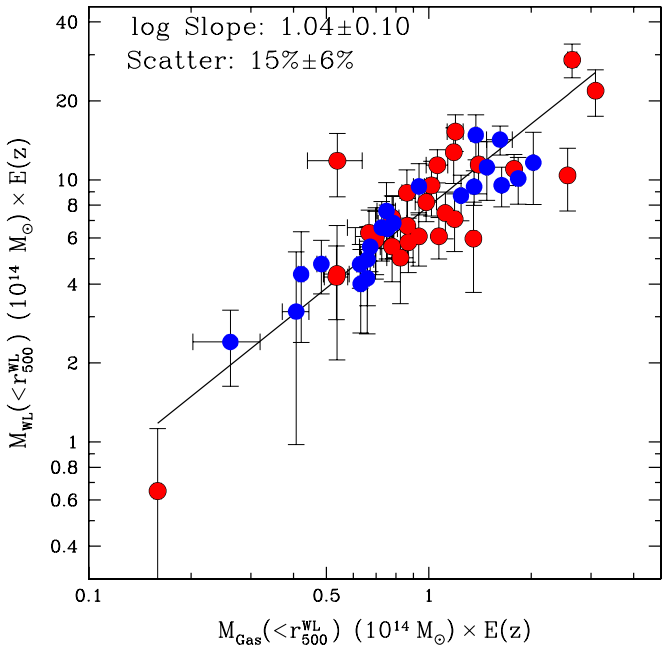

Figure 7. The gas mass–lensing mass relationship at lensing r_{500}. Blue circles show low BCG offset systems and red circles show high BCG offset systems. Most of the low BCG offset systems are also low central entropy clusters.

(A color version of this figure is available in the online journal.)

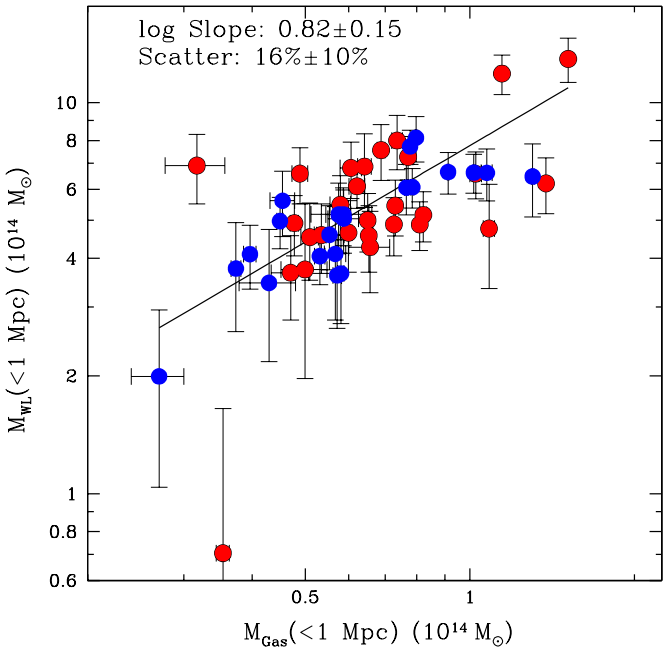

Figure 8. Lensing mass vs. gas mass at a fixed physical radius of 1 Mpc. Blue circles show low BCG offset clusters and red circles show high BCG offset clusters. The relation retains the low scatter of the relations at fixed density contrast.

(A color version of this figure is available in the online journal.)

5.2. Regularity of Cool Core and Low BCG Offset Clusters

Another point of particular importance is the fact that for the cool-core clusters, the 1σ scatter is $<10\%$ (the scatter is $<6\%$ if we cut on BCG offset instead)—these numbers are low enough to be consistent with zero. Simulations and analytical work (e.g., Becker & Kravtsov 2011) show that $\approx 15\%$ is roughly the amount of intrinsic scatter we can expect due to geometric errors

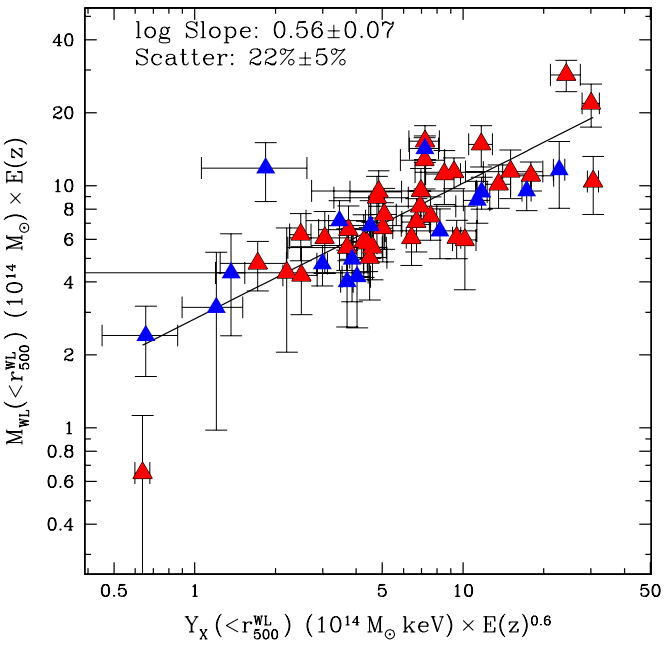

Figure 9. Lensing mass vs. pseudo-pressure Y_X. Blue triangles show cool-core clusters, while red triangles show non-cool-core clusters.

(A color version of this figure is available in the online journal.)

from the assumption of spherical geometry. Thus deviations from spherical symmetry can produce scatter we observe in the cool-core M_{gas}–M_L relation, and as a result, we can begin to claim that we are approaching a full accounting of all sources of systematic error in the mass–observable scaling relation.

We note that the BCG offset works as well as central entropy in identifying the low-scatter subsample. This is an interesting result, because of our four substructure measures, BCG offset is by far the least expensive to calculate, in that it does not require X-ray temperature (spectral) information—a set of X-ray and optical images is sufficient to calculate D_{BCG}. However, it is worth noting that while the low BCG offset and cool-core subsamples have significant overlap, they are not precisely the same, and the two cuts trace two different types of equilibrium (dynamical and thermal, respectively).

Another frequently used mass proxy is Y_X, the pseudo-integrated pressure first pioneered by Kravtsov et al. (2006) and examined by Vikhlinin et al. (2006); being the product of the gas mass and the core-cut temperature at r^{WL}_{500}, Y_X is directly comparable to the integrated Sunyaev–Zel'dovich (SZ) Compton Y parameter (Plagge et al. 2010; Andersson et al. 2011).

We show the Y_X–M_L relation at r^{WL}_{500} for our sample in Figure 9; we find consistency with the expected self-similar slope of 0.6, but slightly higher intrinsic scatter to the gas mass when used as a mass proxy: the overall intrinsic deviation is $\approx 22\% \pm 5\%$ regardless of whether we use the entire sample or the cool-core subsample.

One might be tempted to argue that gas mass is a superior mass proxy to Y_X, not simply because of its ease of calculation and comparable overall intrinsic scatter, but also because of the systematically lower intrinsic scatter that comes about when only cool-core clusters are considered. However, this discrimination between relaxed and non-relaxed clusters is perhaps not optimal in a cosmological context, where uniformity of scatter across the entire sample is important. Where uniformity is most important, Y_X is a superior choice to gas mass, because as

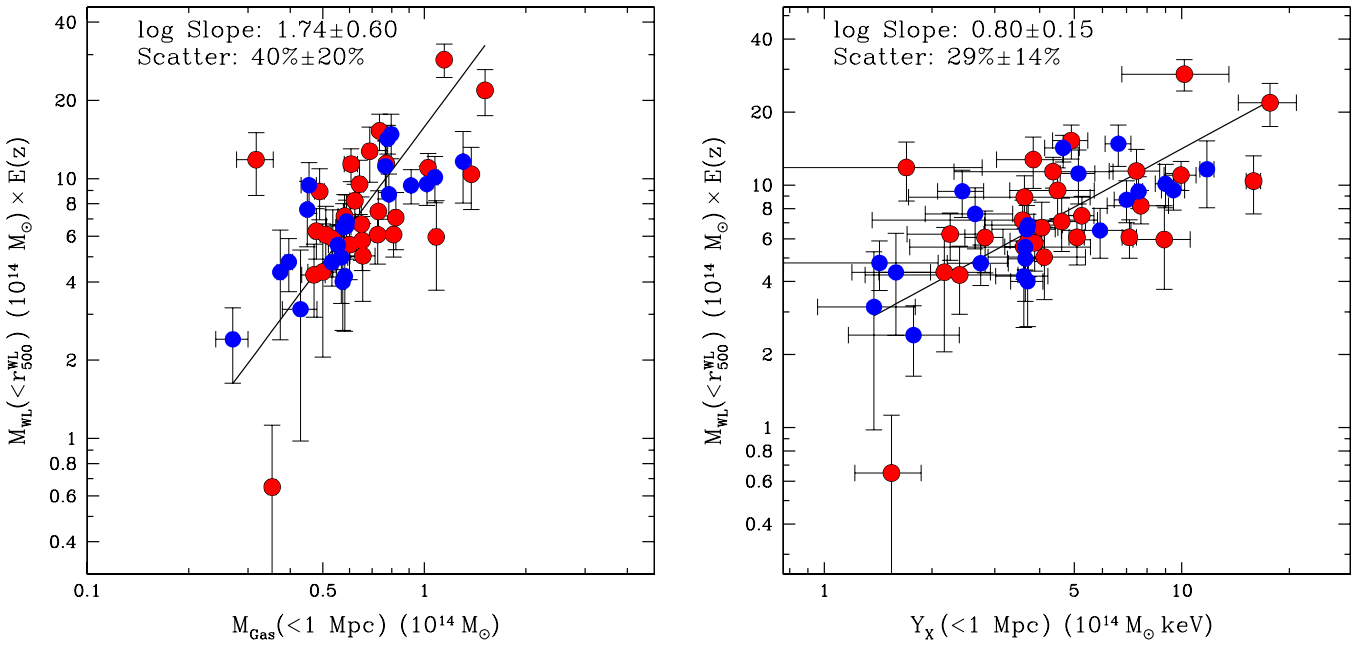

Figure 10. The lensing mass at r_{500} vs. gas mass and Y_X measured at *fixed* radius of 1 Mpc. Blue circles show low BCG offset clusters, while red circles show high BCG offset clusters.

(A color version of this figure is available in the online journal.)

we show in Table 3 it has uniform scatter regardless of cluster central entropy or BCG offset.

Finally, it is instructive to compare Y_X with its radio counterpart, the cylindrically integrated SZ pressure Y_{SZ}. Hoekstra et al. (2012) consider direct correlations between Y_{SZ} from the *Planck* mission and projected weak lensing masses; they find an intrinsic scatter of 12% ± 5% at projected r_{2500}. As a point of comparison, when we conduct a similar exercise on spherically determined Y_X and M_{WL} (both measured at spherical r^{WL}_{2500}), we find an intrinsic scatter of 18% ± 6%, consistent with the Hoekstra et al. (2012) SZ comparison.

5.3. Predicting M^{WL}_{500} with Fixed Aperture Mass Proxies for Surveys

In a blind X-ray survey, the aperture r^{WL}_{500} or even r^{X}_{500} may not be easily available. For cosmology, we still need to know M_{500}. It is therefore useful to investigate whether one can directly predict M^{WL}_{500} without the need to calculate overdensity radii r_Δ for the various X-ray observables. For example, a wide-field all-sky X-ray survey may be able to measure hundreds of thousands of gas masses within fixed physical apertures, but lack the photon statistics to allow for the calculation of X-ray overdensity radii.

In Figure 10 we consider this situation, plotting $M_{WL}(<r^{WL}_{500})$ against gas mass and Y_X measured within a fixed radius of 1 Mpc. As expected, the slopes now deviate from self-similar, and the intrinsic scatter is considerably higher than in Figures 7 and 9. However, interestingly, Y_X exhibits somewhat less scatter (29%) in this "mixed" scaling relation than does gas mass (40%). In surveys with poor photon statistics where no X-ray or weak lensing estimates of r_{500} are readily available, Y_X *measured within a fixed physical aperture* may constitute a better mass proxy, because no separate estimate of X-ray r_{500} is required to use the relations shown in Figure 10. The results are summarized in Table 3.

These data leave us with the perhaps dispiriting result that low (<10%) scatter X-ray mass proxies may be derived either at fixed physical radii, yielding total mass estimates within fixed physical radii; or they may be derived at fixed overdensity radii, yielding total mass estimates within fixed overdensities. But it seems difficult to achieve very low scatter without either committing to fixed physical radii (straightforward to measure, but more difficult to use for cosmology) or to fixed overdensity radii (difficult to measure, but more useful for cosmology) in both axes.

5.4. Lack of Correlation with Substructure Measures

We have already argued that the intrinsic scatter in the lensing mass to X-ray observable relations is potentially fully accounted for by the triaxiality of the clusters; nevertheless, it is still useful to consider whether the scatter in such relation may be further minimized via correlation with measures of substructure, at least as an empirical means to gauge the effect of this triaxiality. However, we find that none of the substructure measures—BCG offset, central entropy, centroid shift variance, or power ratio—have any significant correlation with residuals in the mass–observable relation. We note that Marrone et al. (2012) did find a residual correlation with BCG *ellipticity* in the relationship between weak lensing mass and the integrated SZ effect signal Y_{SZ}. We examine a similar relation in Section 6.2.

It follows from this lack of correlation that the M_x/M_{WL} ratio itself is not correlated with morphological measures such as centroid shift or power ratio, either. Rasia et al. (2012) consider a similar question; they examine whether the ratio of the X-ray mass to the true mass is correlated with centroid shift or power ratio. They find a weak correlation between this ratio and the substructure measures, with a Pearson rank coefficient of −0.2 to −0.3, significant at 2σ. We do not observe such a correlation, most likely because we do not measure the X-ray to true mass ratio, but rather the X-ray to weak lensing mass ratio, the latter of which has its own intrinsic scatter.

In our present sample, then, it is possible to minimize the scatter in the mass–observable relation by conducting a cut on

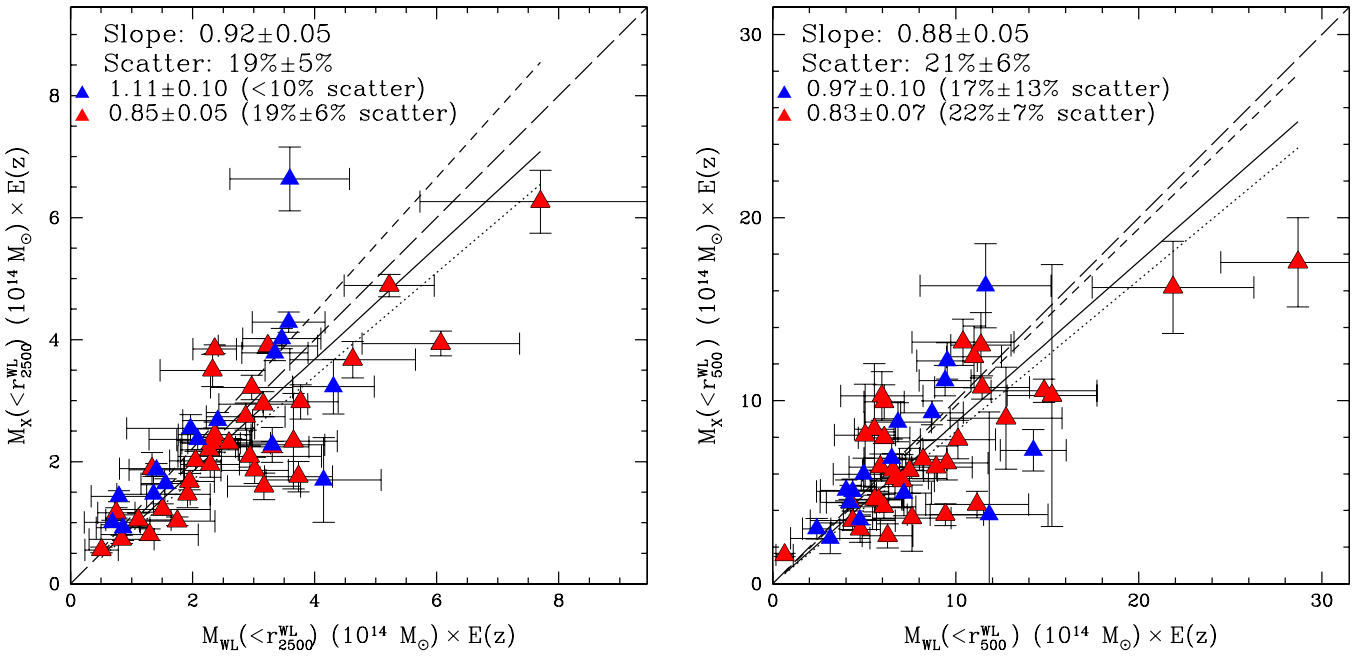

Figure 11. The relationship between hydrostatic mass and lensing mass at r^{WL}_{2500} (left) and r^{WL}_{500} (right). Blue triangles show cool-core clusters and red triangles show non-cool-core clusters. Cool-core clusters tend to have hydrostatic masses that agree with lensing masses; non-cool-core clusters tend to exhibit the hydrostatic mass underestimate. The solid line indicates the best fit, the long-dashed line indicates the line of equality, the short-dashed line corresponds to the cool-core clusters, and the dotted line corresponds to the non-cool-core clusters.

(A color version of this figure is available in the online journal.)

central entropy, but it is not possible to "correct" this scatter for the non-cool-core clusters by utilizing any of the four substructure quantifiers we consider or even BCG ellipticity.

6. DEVIATIONS FROM HYDROSTATIC EQUILIBRIUM

6.1. Hydrostatic Mass Underestimate

Mahdavi et al. (2008) argued that a subsample of the clusters discussed here have X-ray masses at r^{WL}_{500} that are on the average 15% lower than their lensing masses at r^{WL}_{500}. This discrepancy may be attributed to deviations from HSE due to residual gas motions and incomplete thermalization of the ICM; the fact that hydrostatic masses tend to underestimate the true mass by 10%–20% was first discussed by Evrard (1990) and continues to be important in grid-based simulations (e.g., Lau et al. 2009; Nelson et al. 2012), SPH simulations (e.g., Rasia et al. 2006; Battaglia et al. 2012; Rasia et al. 2012), and observations of distant clusters (Andersson et al. 2011; Jee et al. 2011). Biases in gravitational lensing masses could in principle also affect the X-ray to weak lensing mass ratio; such systematic biases are only ≈5%–10%, but would have the effect of increasing the X-ray to weak lensing mass ratio (e.g., Becker & Kravtsov 2011). Note that in recent *N*-body hydrodynamical simulations, even though the hydrostatic bias (10%–15%) is roughly twice the level of the weak lensing bias, the scatter about this bias is larger by a factor of two for weak lensing masses than for the hydrostatic masses (Meneghetti et al. 2010; Rasia et al. 2012; Nelson et al. 2012).

It is worth pointing out, however, that the technique we use for our lensing mass measurements should yield lower bias than suggested by these simulations. The technique achieves this lower bias of 3%–4% (rather than the expected bias of 5%–10%) by omitting the regions of the shear map that are most susceptible, at the cost of increased statistical uncertainty. We refer the reader to Hoekstra et al. (2012) for details.

In Figure 11 we extend our results to the full sample of 50 clusters. The larger size of the sample allows us to resolve differences between cool-core and non-cool-core clusters. We find that cool-core clusters and non-cool-core clusters do not exhibit the same level of departure from HSE.

Cool-core clusters have hydrostatic masses that are proportional to their weak lensing masses at all radii. The M_X–M_L relation for this subsample has a small scatter (<20%), about the right level for all the scatter to be accounted for by triaxiality. Overall, we find that cool-core clusters are consistent with having no difference between their X-ray and weak lensing masses.

The picture is dramatically different for non-cool-core clusters. In these systems, we find a roughly constant hydrostatic mass to lensing mass ratio of 80%, regardless of whether we look at r^{WL}_{500} or r^{WL}_{2500}. Our results are consistent with *N*-body gas dynamical simulations as shown in Figure 12 and Table 4. Broadly, these results are consistent with the hydrostatic mass underestimates predicted by gas dynamical simulations that account for unthermalized gas, such as in Nagai et al. (2007), Jeltema et al. (2008), and Lau et al. (2009). We find that the non-cool-core clusters populate the lower end of the region allowed by these simulations, whereas the cool-core clusters populate the region where X-ray and true mass agree within 10%. Of these simulations Jeltema et al. (2008) is the most consistent with our measured 20% average mass underestimate for disturbed systems.

6.2. Correlation with BCG Ellipticity

Finally, we consider the question of whether BCG ellipticity is correlated with differences between hydrostatic and weak

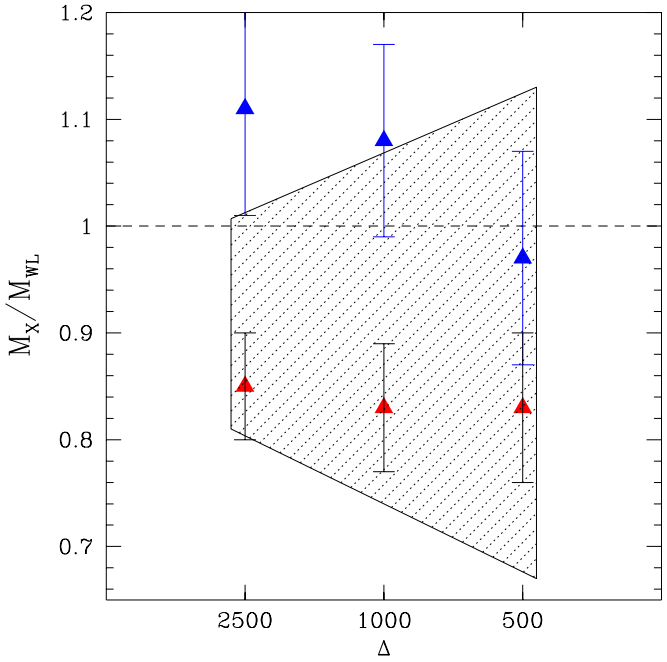

Figure 12. The X-ray to weak lensing mass ratio as a function of density contrast for cool-core systems (blue triangles) and non-cool-core systems (red triangles). The error bars are not independent because the data within r_{2500} also contribute to the measurement at r_{500}. The shaded region shows the range of X-ray cluster mass underestimate as determined by Lau et al. (2009).

(A color version of this figure is available in the online journal.)

lensing masses. Such a correlation is suggested by Marrone et al. (2012), who use the integrated Compton parameter $Y_{\rm sph}$ as a mass proxy. In Figure 13, we show $M_X/M_{\rm WL}$ at r_{2500} and r_{500}, plotted against CFHT ellipticities measured at 30 kpc. We find that cool-core systems are consistent with $M_X/M_L = 1$ ($\chi^2/\nu = 18/14$), whereas non-cool-core systems are definitively not consistent with $M_x/M_L = 1$ ($\chi^2/\nu = 70/29$).

Table 4
X-Ray to Weak Lensing Mass Ratios

Contrast	Sample	M_X/M_L	Fractional Scatter in M_X at Fixed M_L
$r^{\rm WL}_{2500}$	All	0.92 ± 0.05	0.19 ± 0.05
	$K_0 < 70$ keV cm^2	1.11 ± 0.10	$<10\%$
	$K_0 > 70$ keV cm^2	0.85 ± 0.05	0.19 ± 0.06
	$D_{\rm BCG} < 0.01$ Mpc	1.04 ± 0.07	<0.15
	$D_{\rm BCG} > 0.01$ Mpc	0.81 ± 0.07	0.24 ± 0.07
$r^{\rm WL}_{1000}$	All	0.89 ± 0.05	0.20 ± 0.05
	$K_0 < 70$ keV cm^2	1.08 ± 0.09	$<9\%$
	$K_0 > 70$ keV cm^2	0.83 ± 0.06	0.20 ± 0.06
	$D_{\rm BCG} < 0.01$ Mpc	0.97 ± 0.07	0.13 ± 0.10
	$D_{\rm BCG} > 0.01$ Mpc	0.84 ± 0.06	0.22 ± 0.07
$r^{\rm WL}_{500}$	All	0.88 ± 0.05	0.21 ± 0.06
	$K_0 < 70$ keV cm^2	0.97 ± 0.10	0.17 ± 0.13
	$K_0 > 70$ keV cm^2	0.83 ± 0.07	0.22 ± 0.07
	$D_{\rm BCG} < 0.01$ Mpc	0.85 ± 0.09	0.22 ± 0.11
	$D_{\rm BCG} > 0.01$ Mpc	0.89 ± 0.07	0.20 ± 0.08

Therefore, for non-cool-core systems, we find a good correlation between BCG ellipticity and the X-ray to weak lensing ratio at $r^{\rm WL}_{2500}$, and a weak correlation at r_{500}. While this is similar to the trend found by Marrone et al. (2012) for $Y_{\rm sph}$, there is a difference in that our cool-core systems do not appear to participate in the correlation. Furthermore, also in apparent contrast with Marrone et al. (2012), our correlation becomes less significant at $r^{\rm WL}_{500}$. We interpret this result as suggesting that while cluster orientation plays some role in low X-ray to weak lensing mass ratios, it is not the only agent at work in this complex relationship (indeed, the hydrostatic mass underestimate must also play a role).

We note that it is not altogether surprising that the trend of ellipticity with M_X/M_L for cool-core clusters is insignificant. We have shown in Section 6 that our X-ray and weak lensing

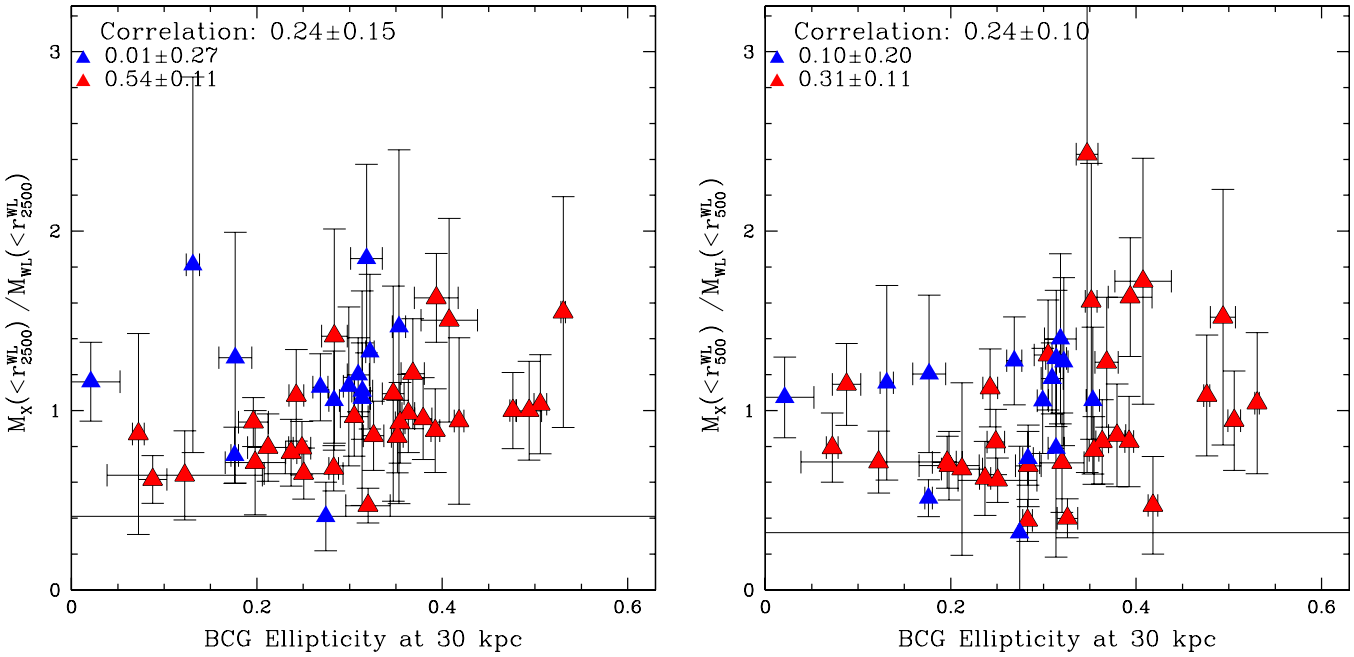

Figure 13. The X-ray to weak lensing mass ratio as a function of BCG ellipticity for 43 BCGs with measurable ellipticities at 30 kpc. The largest error bar in ellipticity belongs to CL0024. Shown are non-cool-core systems (red triangles) and cool-core systems (blue triangles). The correlation is significant only for the non-cool-core systems at r_{2500}; there is a marginal correlation at r_{500}. Cool-core systems do not participate in the trend.

(A color version of this figure is available in the online journal.)

masses are consistent for this sub-population (in contrast, Marrone et al. (2012) contained several undisturbed clusters with significant $Y_{\rm sph}$ to weak lensing mass discrepancies).

Furthermore, it is difficult to untangle the effects of elongation along the line of sight (which would chiefly bias weak lensing masses high) and non-hydrostatic gas (which would chiefly bias the X-ray masses low). We also stress that the trend is altogether absent at r_{500}. However, empirically, we can point out that the non-cool-core clusters with the highest ellipticities have consistent X-ray and weak lensing masses, something corroborated by Marrone et al. (2012).

7. CONCLUSION

We examine archival X-ray data on a sample of 50 clusters of galaxies; most of the clusters have *Chandra* data, while roughly half have *XMM-Newton* data of good quality. All clusters have CFHT weak gravitational lensing data from either the CFH12k or the Megacam instruments.

In attempting to combine *Chandra* and *XMM-Newton* data to maximize both effective area and spatial resolution, we confirm previously reported systematic calibration differences between the two observatories. Using multiple calibration releases, we find a 15% systematic difference in hydrostatic masses between *Chandra* and *XMM-Newton*. Reassuringly, there is no intrinsic scatter between the masses for the two observatories, indicating that the issue is merely a matter of overall gain calibration and not a more serious spatially dependent issue. We develop an effective area correction that revises *Chandra* masses downward into agreement with *XMM-Newton* masses. This correction is only valid for high-temperature ($\gtrsim$5 keV) clusters such as ours; at lower temperatures, the two observatories are more consistent due to the abundant prominence of X-ray lines.

Using the L_X–T_X relation, we find that our sample is consistent with being randomly drawn from the same parent population as samples with well-understood selection functions, such as HIFLUGCS (Reiprich & Böhringer 2002) and MACS (Ebeling et al. 2010).

We examine several measures of substructure, including central entropy, BCG to X-ray peak offset, centroid shift variance, and power ratios. There is a significant correlation among all the substructure measures. The most strikingly correlated quantities are the BCG to X-ray peak offset (in Mpc) and the central entropy measured at a radius of 20 kpc. The hint of bimodality in the joint 2D distribution of the BCG offset and central entropy indicates a complex connection between the thermal and dynamical relaxation times of galaxy clusters.

Gas mass is by far the most robust predictor of weak lensing mass, with <10% scatter for cool-core clusters and 14% ± 6% scatter for the sample overall. It is followed by the X-ray pseudo-pressure, Y_X, which has 23%±6% intrinsic scatter for both cool-core clusters and the sample overall. The mass–temperature relationship has even higher scatter, 43% ± 21% for the sample overall. All scaling relations have slopes that are consistent with the expected self-similar value. We also find that core-excised X-ray luminosity is somewhat better than temperature at predicting weak lensing mass, yielding 28% ± 18% intrinsic scatter for relaxed systems.

By comparing hydrostatic and weak gravitational lensing masses, we extend our earlier detection (Mahdavi et al. 2008) of non-hydrostatic gas, with associated deviations from HSE, in X-ray clusters of galaxies. We are able to quantify the hydrostatic mass underestimate separately for cool-core and non-cool-core clusters. We find that cool-core clusters exhibit little or no difference between their weak lensing and X-ray masses; the hydrostatic mass underestimate is consistent with 0% at both $r_{2500}^{\rm WL}$ and at $r_{500}^{\rm WL}$. Non cool-core clusters, on the other hand, have fairly consistent, ≈20% ± 10%, underestimates between the same radii. This is broadly consistent with *N*-body gas dynamical simulations of unthermalized gas.

Except for the non-core-cut L_X–T_X relation, we do not find a significant correlation between the *residuals* in a given scaling relation and any of our four substructure measures (central entropy, BCG offset, centroid shift variance, or $P3/P0$ power ratio). We interpret this result as indicating that it is not possible to reduce the intrinsic scatter in a scaling relation (other than the L_X–T_X relation) by applying corrections based on substructure measures to individual clusters. In essence, clusters of galaxies have "forgotten" the sources of their departures from self-similarity. This lack of correlation suggests that we may have accounted for most if not all of the parameters that could affect the cluster selection function for cosmological surveys, and that few if any "hidden" parameters remain.

However, we do find a partial trend with cluster ellipticity: cool-core clusters have consistent X-ray and weak lensing masses at $r_{2500}^{\rm WL}$, whereas non-cool-core clusters have increasing $M_X(< r_{2500}^{\rm WL})/M_L(< r_{2500}^{\rm WL})$ with BCG ellipticity at 30 kpc. Clusters with low-ellipticity BCGs are the most likely to have mismatched X-ray and weak lensing masses, while clusters with higher ellipticity are more likely to have concordant X-ray and weak lensing masses. We leave it to future studies to determine which combination of X-ray non-hydrostatic bias and lensing projection bias is contributing to this trend.

We emphasize that the X-ray peak to BCG location offset is perhaps the most efficient among our inspected substructure measures. Selecting clusters based on low BCG offset is sufficient to guarantee scatter consistent with zero in the gas mass–lensing mass relation, at least for a sample as large as or larger than ours.

In summary, we find that cool-core clusters with $K_0 <$ 70 keV cm^2 or BCG offset <0.01 Mpc are extremely well-behaved and regular systems with respect to their X-ray and lensing properties. However, it should be noted that the two cuts do not select the same subsamples, because low BCG offset is indicative of the dynamical equilibrium, whereas low central entropy is a result of thermal equilibrium. While there are clusters that are in both thermal and dynamical equilibrium, the overlap is not perfect.

Clusters with $K_0 >$ 70 keV cm^2 show some intriguing properties—such as tightly correlated $P3/P0$ power ratios and BCG offsets, a linear correlation between M_X/M_L and ellipticity, and consistently low X-ray to weak lensing mass ratios—but larger samples and more careful theoretical studies are required before we can learn how to use these relations to gain greater physical insight into their evolution.

The authors would like to acknowledge productive discussions with Steve Allen, Hans Böhringer, Dick Bond, Maruša Bradač, Megan Donahue, Stefano Ettori, Gus Evrard, Fabio Gastaldello, Andrey Kravtsov, Dan Marrone, Daisuke Nagai, Trevor Ponman, Graham Smith, David Spergel, and Mark Voit. The anonymous referee made comments which improved the paper. A.M. and T.J. were supported by NASA through Chandra award No. AR0-11016A, issued by the Chandra X-ray Observatory Center, which is operated by the Smithsonian Astrophysical Observatory for and on behalf of NASA under contract NAS8-03060. A.M. was also supported through NASA

ADAP grant 11-ADAP11-0270. A.B. would also like to acknowledge research funding from NSERC Canada through its Discovery Grant program as well as support provided by J. Criswick. H.H. acknowledges support from the Netherlands Organisation for Scientific Research (NWO) through VIDI grant 639.042.814; H.H. and C.B. acknowledge support from Marie Curie IRG Grant 230924. A.M. and A.B. acknowledge an especially productive time at the Kavli Institute for Theoretical Physics, where this research was supported in part by the National Science Foundation under grant No. NSF PHY11-25915.

REFERENCES

Allen, S. W., Evrard, A. E., & Mantz, A. B. 2011, ARA&A, 49, 409
Andersson, K., Benson, B. A., Ade, P. A. R., et al. 2011, ApJ, 738, 48
Arnaud, M., Pointecouteau, E., & Pratt, G. W. 2007, A&A, 474, L37
Bahé, Y. M., McCarthy, I. G., & King, L. J. 2012, MNRAS, 421, 1073
Battaglia, N., Bond, J. R., Pfrommer, C., & Sievers, J. L. 2012, ApJ, 758, 74
Becker, M. R., & Kravtsov, A. V. 2011, ApJ, 740, 25
Bildfell, C., Hoekstra, H., Babul, A., & Mahdavi, A. 2008, MNRAS, 389, 1637
Bildfell, C., Hoekstra, H., Babul, A., et al. 2012, MNRAS, 425, 204
Böhringer, H., Pratt, G. W., Arnaud, M., et al. 2010, A&A, 514, A32
Buote, D. A., & Tsai, J. C. 1995, ApJ, 452, 522
Carlberg, R. G., Yee, H. K. C., Ellingson, E., et al. 1996, ApJ, 462, 32
Donahue, M., Stocke, J. T., & Gioia, I. M. 1992, ApJ, 385, 49
Duffy, A. R., Schaye, J., Kay, S. T., & Dalla Vecchia, C. 2008, MNRAS, 390, L64
Ebeling, H., Edge, A. C., Mantz, A., et al. 2010, MNRAS, 407, 83
Ebeling, H., Jones, L. R., Perlman, E., et al. 2000, ApJ, 534, 133
Evrard, A. E. 1990, ApJ, 363, 349
Fabian, A. C., Crawford, C. S., Edge, A. C., & Mushotzky, R. F. 1994, MNRAS, 267, 779
Feroz, F., & Hobson, M. P. 2012, MNRAS, 420, 596
Fischer, P., & Tyson, J. A. 1997, AJ, 114, 14
Gioia, I. M., Maccacaro, T., Schild, R. E., et al. 1990, ApJS, 72, 567
Girardi, M., Fadda, D., Escalera, E., et al. 1997, ApJ, 490, 56
Henry, J. P., Evrard, A. E., Hoekstra, H., Babul, A., & Mahdavi, A. 2009, ApJ, 691, 1307
High, F. W., Hoekstra, H., Leethochawalit, N., et al. 2012, ApJ, 758, 68
Hoekstra, H. 2007, MNRAS, 379, 317
Hoekstra, H., Mahdavi, A., Babul, A., & Bildfell, C. 2012, MNRAS, 427, 1298
Hogg, D. W., Bovy, J., & Lang, D. 2010, arXiv:1008.4686
Horner, D. J. 2001, PhD thesis, Univ. Maryland College Park
Jee, M. J., Dawson, K. S., Hoekstra, H., et al. 2011, ApJ, 737, 59
Jee, M. J., Mahdavi, A., Hoekstra, H., et al. 2012, ApJ, 747, 96
Jeltema, T. E., Canizares, C. R., Bautz, M. W., & Buote, D. A. 2005, ApJ, 624, 606
Jeltema, T. E., Hallman, E. J., Burns, J. O., & Motl, P. M. 2008, ApJ, 681, 167
Kaiser, N. 1991, ApJ, 383, 104
Kravtsov, A. V., & Borgani, S. 2012, ARA&A, 50, 353
Kravtsov, A. V., Vikhlinin, A., & Nagai, D. 2006, ApJ, 650, 128
Lau, E. T., Kravtsov, A. V., & Nagai, D. 2009, ApJ, 705, 1129
Mahdavi, A., Hoekstra, H., Babul, A., & Henry, J. P. 2008, MNRAS, 384, 1567
Mahdavi, A., Hoekstra, H., Babul, A., et al. 2007, ApJ, 664, 162
Mantz, A., Allen, S. W., & Rapetti, D. 2010, MNRAS, 406, 1805
Marrone, D. P., Smith, G. P., Okabe, N., et al. 2012, ApJ, 754, 119
Maughan, B. J., Giles, P. A., Randall, S. W., Jones, C., & Forman, W. R. 2012, MNRAS, 421, 1583
Mazzotta, P., Rasia, E., Moscardini, L., & Tormen, G. 2004, MNRAS, 354, 10
McCarthy, I. G., Balogh, M. L., Babul, A., Poole, G. B., & Horner, D. J. 2004, ApJ, 613, 811
Meneghetti, M., Rasia, E., Merten, J., et al. 2010, A&A, 514, A93
Miralda-Escude, J., & Babul, A. 1995, ApJ, 449, 18
Mittal, R., Hicks, A., Reiprich, T. H., & Jaritz, V. 2011, A&A, 532, A133
Morandi, A., Ettori, S., & Moscardini, L. 2007, MNRAS, 379, 518
Nagai, D., Vikhlinin, A., & Kravtsov, A. V. 2007, ApJ, 655, 98
Navarro, J. F., Frenk, C. S., & White, S. D. M. 1997, ApJ, 490, 493
Nelson, K., Rudd, D. H., Shaw, L., & Nagai, D. 2012, ApJ, 751, 121
Nevalainen, J., David, L., & Guainazzi, M. 2010, A&A, 523, A22
Okabe, N., Zhang, Y., Finoguenov, A., et al. 2010, ApJ, 721, 875
O'Sullivan, E., Giacintucci, S., Babul, A., et al. 2012, MNRAS, 424, 2971
Ota, N., Pointecouteau, E., Hattori, M., & Mitsuda, K. 2004, ApJ, 601, 120
Pedersen, K., & Dahle, H. 2007, ApJ, 667, 26
Pesce, J. E., Fabian, A. C., Edge, A. C., & Johnstone, R. M. 1990, MNRAS, 244, 58
Pizzolato, F., Molendi, S., Ghizzardi, S., & De Grandi, S. 2003, ApJ, 592, 62
Plagge, T., Benson, B. A., Ade, P. A. R., et al. 2010, ApJ, 716, 1118
Poole, G. B., Babul, A., McCarthy, I. G., et al. 2007, MNRAS, 380, 437
Poole, G. B., Fardal, M. A., Babul, A., et al. 2006, MNRAS, 373, 881
Pratt, G. W., Arnaud, M., Piffaretti, R., et al. 2010, A&A, 511, A85
Rasia, E., Ettori, S., Moscardini, L., et al. 2006, MNRAS, 369, 2013
Rasia, E., Mazzotta, P., Borgani, S., et al. 2005, ApJL, 618, L1
Rasia, E., Meneghetti, M., Martino, R., et al. 2012, NJPh, 14, 055018
Reese, E. D., Kawahara, H., Kitayama, T., et al. 2010, ApJ, 721, 653
Reiprich, T. H., & Böhringer, H. 2002, ApJ, 567, 716
Sanderson, A. J. R., & Ponman, T. J. 2010, MNRAS, 402, 65
Shaw, L. D., Nagai, D., Bhattacharya, S., & Lau, E. T. 2010, ApJ, 725, 1452
Snowden, S. L., Mushotzky, R. F., Kuntz, K. D., & Davis, D. S. 2008, A&A, 478, 615
Tsujimoto, M., Guainazzi, M., Plucinsky, P. P., et al. 2011, A&A, 525, A25
Ventimiglia, D. A., Voit, G. M., Donahue, M., & Ameglio, S. 2008, ApJ, 685, 118
Vikhlinin, A. 2006, ApJ, 640, 710
Vikhlinin, A., Burenin, R. A., Ebeling, H., et al. 2009a, ApJ, 692, 1033
Vikhlinin, A., Kravtsov, A., Forman, W., et al. 2006, ApJ, 640, 691
Vikhlinin, A., Kravtsov, A. V., Burenin, R. A., et al. 2009b, ApJ, 692, 1060
Yee, H. K. C., Ellingson, E., & Carlberg, R. G. 1996, ApJS, 102, 269
Zhang, Y.-Y., Finoguenov, A., Böhringer, H., et al. 2008, A&A, 482, 451

The Astrophysical Journal, 794:175 (3pp), 2014 October 20 doi:10.1088/0004-637X/794/2/175

ERRATUM: "JOINT ANALYSIS OF CLUSTER OBSERVATIONS. II. *CHANDRA*/*XMM-NEWTON* X-RAY AND WEAK LENSING SCALING RELATIONS FOR A SAMPLE OF 50 RICH CLUSTERS OF GALAXIES" (2013, ApJ, 767, 116)

Andisheh Mahdavi[1], Henk Hoekstra[2], Arif Babul[3], Chris Bildfell[3], Tesla Jeltema[4], and J. Patrick Henry[5]
[1] Department of Physics and Astronomy, San Francisco State University, San Francisco, CA 94131, USA
[2] Leiden Observatory, Leiden University, Niels Bohrweg 2, NL-2333 CA Leiden, The Netherlands
[3] Department of Physics and Astronomy, University of Victoria, Victoria, BC V8W 3P6, Canada
[4] Santa Cruz Institute for Particle Physics, UC Santa Cruz, 1156 High Street, Santa Cruz, CA 95064, USA
[5] Institute for Astronomy, 2680 Woodlawn Drive, Honolulu, HI 96822, USA
Received 2014 July 28; published 2014 October 7

The published version of the article "Joint Analysis of Cluster Observations. II. *Chandra*/*XMM-Newton* X-ray and Weak Lensing Scaling Relations for a Sample of 50 Rich Clusters of Galaxies" contained an error in the bolometric correction factor in the reported X-ray luminosities. In addition, Table 1 contained thermodynamic quantities reported at r_{2500} instead of r_{500}. No other aspects of the analysis were affected. We present a table with updated quantities and fit results.

In the published version of this article, we applied an incorrect bolometric bandpass correction factor to the X-ray flux of all clusters, resulting in bolometric X-ray luminosities that were too high throughout the entire analysis. Since this was a problem only with the bandpass correction factor, none of the other results of the paper were affected. In addition, Table 1 of the published article reported luminosities and temperatures at an aperture of r_{2500} instead of r_{500}.

Here we present updated luminosities and mass–luminosity scaling relations (Table 3) which take the correct bolometric correction factor into account. Note that the *Chandra* and *XMM-Newton Observatory* calibrations used are the same one as in the published article. These updated numbers are also present on the Web site of the paper, http://sfstar.sfsu.edu/jaco. Since the error was roughly a constant factor applied to L_X, only the intercepts of the L_X relations have changed substantially; the slopes and intrinsic scatters of these relations are still within the originally reported limits.

A revision of the entire analysis with the latest calibration releases from both observatories will appear in a forthcoming paper.

Table 1
Basic Properties of the Sample

Cluster Name	R.A. (J2000)	Decl. (J2000)	z	*Chandra* ObsID	Exposure (s)	*XMM-Newton* ObsID	Exposure (s)	$L_{X,\mathrm{all,bol},500}$ (keV)	$T_{\mathrm{all},500}$ (10^{45} erg s^{-1})
3C295	14:11:20.52	+52:12:09.9	0.464	2254	87914	...	...	1.16 ± 0.02	5.7 ± 0.3
Abell0068	00:37:06.65	+09:09:24.0	0.255	3250	9986	0084230201	14068	1.43 ± 0.02	6.3 ± 0.4
Abell0115N	00:55:50.37	+26:24:36.6	0.197	3233	49719	0203220101	21393	1.11 ± 0.01	5.3 ± 0.2
Abell0115S	00:56:00.17	+26:20:29.5	0.197	3233	49719	0203220101	21309	1.17 ± 0.01	5.4 ± 0.3
Abell0209	01:31:53.42	−13:36:46.3	0.206	3579	9986	0084230301	11219	1.77 ± 0.02	7.0 ± 0.4
Abell0222	01:37:34.25	−12:59:30.8	0.207	4967	45078	0502020201	23178	0.50 ± 0.01	4.1 ± 0.3
Abell0223S	01:37:56.06	−12:49:12.8	0.207	4967	45078	0502020201	23206	0.62 ± 0.01	6.3 ± 0.4
Abell0267	01:52:42.38	+01:00:48.0	0.231	3580	19624	0084230401	10421	1.15 ± 0.03	6.5 ± 0.5
Abell0370	02:39:53.18	−01:34:34.9	0.375	515	68532	...	...	1.55 ± 0.06	7.2 ± 0.6
Abell0383	02:48:03.33	−03:31:45.1	0.187	2320	19285	0084230501	20237	0.96 ± 0.01	3.7 ± 0.1
Abell0520	04:54:10.10	+02:55:18.3	0.199	4215	66274	0201510101	21915	1.58 ± 0.02	7.3 ± 0.2
Abell0521	04:54:06.30	−10:13:16.9	0.253	901	38626	...	...	1.37 ± 0.02	5.9 ± 0.3
Abell0586	07:32:20.16	+31:37:56.6	0.171	530	10043	...	...	1.19 ± 0.02	5.1 ± 0.4
Abell0611	08:00:56.96	+36:03:22.0	0.288	3194	36114	...	...	1.61 ± 0.05	8.7 ± 0.6
Abell0697	08:42:57.29	+36:21:56.2	0.282	4217	19516	...	...	3.15 ± 0.07	10.3 ± 0.7
Abell0851	09:43:00.39	+46:59:20.4	0.407	...	...	0106460101	15731	0.93 ± 0.03	6.1 ± 0.4
Abell0959	10:17:35.61	+59:33:53.4	0.286	...	...	0406630201	4134	0.58 ± 0.03	6.0 ± 1.7
Abell0963	10:17:03.63	+39:02:48.3	0.206	903	36289	0084230701	17234	1.57 ± 0.01	6.2 ± 0.2
Abell1689	13:11:29.52	−01:20:29.8	0.183	6930	76144	0093030101	24457	4.48 ± 0.02	10.9 ± 0.2
Abell1758E	13:32:46.43	+50:32:25.9	0.279	2213	55220	...	...	2.33 ± 0.06	8.9 ± 0.6
Abell1758W	13:32:38.70	+50:33:23.0	0.279	2213	55220	...	...	1.46 ± 0.06	8.7 ± 1.0
Abell1763	13:35:18.16	+40:59:57.7	0.223	3591	19595	0084230901	8852	1.91 ± 0.03	6.3 ± 0.2
Abell1835	14:01:01.90	+02:52:42.7	0.253	6880	117918	0098010101	16021	4.51 ± 0.02	7.1 ± 0.1
Abell1914	14:26:02.80	+37:49:27.3	0.171	3593	18865	0112230201	17025	2.97 ± 0.02	9.7 ± 0.2
Abell1942	14:38:21.90	+03:40:12.9	0.224	3290	55716	...	...	0.33 ± 0.01	4.0 ± 0.3
Abell2104	15:40:08.09	−03:18:16.5	0.153	895	49199	...	...	2.32 ± 0.04	5.8 ± 0.3
Abell2111	15:39:41.74	+34:25:01.9	0.229	544	10299	...	...	0.91 ± 0.03	5.6 ± 0.7
Abell2163	16:15:46.05	−06:09:02.6	0.203	1653	71148	...	...	6.45 ± 0.10	11.5 ± 0.7
Abell2204	16:32:46.92	+05:34:32.4	0.152	7940	77141	0306490201	13093	3.99 ± 0.01	7.6 ± 0.1
Abell2218	16:35:50.89	+66:12:36.9	0.176	1666	30693	0112980101	13111	1.28 ± 0.02	6.6 ± 0.2
Abell2219	16:40:20.20	+46:42:35.3	0.226	896	42295	...	...	6.45 ± 0.08	8.3 ± 0.3
Abell2259	17:20:07.75	+27:40:14.7	0.164	3245	9986	...	...	0.77 ± 0.02	5.0 ± 0.3
Abell2261	17:22:27.12	+32:07:58.9	0.224	5007	24316	...	...	2.59 ± 0.03	5.6 ± 0.3
Abell2390	21:53:36.82	+17:41:44.7	0.228	4193	93782	0111270101	8100	5.99 ± 0.03	10.1 ± 0.3
Abell2537	23:08:22.23	−02:11:30.3	0.295	4962	36193	0205330501	6267	1.37 ± 0.03	6.9 ± 0.7
CL0024.0+1652	00:26:35.94	+17:09:46.2	0.390	929	39417	...	...	0.34 ± 0.02	4.5 ± 0.8
MACSJ0717.5+3745	07:17:31.39	+37:45:24.8	0.548	4200	58912	...	...	5.55 ± 0.12	11.6 ± 0.7
MACSJ0913.7+4056	09:13:45.49	+40:56:28.7	0.442	10445	76159	...	...	1.99 ± 0.04	6.0 ± 0.2
MS0015.9+1609	00:18:33.74	+16:26:09.0	0.541	520	67410	0111000101	22477	3.73 ± 0.10	9.5 ± 0.6
MS0440.5+0204	04:43:09.99	+02:10:19.3	0.190	4196	22262	...	...	0.33 ± 0.01	3.3 ± 0.3
MS0451.6-0305	04:54:11.24	−03:00:57.3	0.550	902	43420	...	...	3.25 ± 0.12	9.2 ± 0.8
MS0906.5+1110	09:09:12.73	+10:58:28.4	0.174	924	29752	...	...	1.10 ± 0.02	5.6 ± 0.3
MS1008.1-1224	10:10:32.52	−12:39:53.1	0.301	926	25222	...	...	0.77 ± 0.02	5.9 ± 0.5
MS1231.3+1542	12:33:55.01	+15:26:02.3	0.233	...	...	0404120101	26520	0.29 ± 0.01	4.5 ± 0.2
MS1358.1+6245	13:59:50.56	+62:31:05.3	0.328	516	50989	...	...	1.19 ± 0.03	6.2 ± 0.5
MS1455.0+2232	14:57:15.05	+22:20:33.2	0.258	4192	91626	0108670201	22571	1.84 ± 0.01	4.4 ± 0.1
MS1512.4+3647	15:14:22.47	+36:36:20.9	0.372	800	36400	...	...	0.48 ± 0.02	3.1 ± 0.2
MS1621.5+2640	16:23:35.05	+26:34:22.1	0.426	546	30062	...	...	0.89 ± 0.04	6.9 ± 0.8
RXJ1347.5−1145	13:47:30.59	−11:45:09.8	0.451	3592	57458	0112960101	21712	10.96 ± 0.18	12.1 ± 0.4
RXJ1524.6+0957	15:24:38.85	+09:57:41.8	0.520	1664	49849	...	...	0.41 ± 0.03	4.7 ± 1.2

Table 3
Mass Proxy Fits with Lognormal Intrinsic Scatter

Proxy	Proxy Aperture	$M_{\rm WL}$ Aperture	Sample	Log Slope	Log Intercept	Fractional Scatter in $M_{\rm WL}$ at Fixed Proxy
Relations at fixed overdensity in proxy and mass						
$T_X^{\rm cut}/8$ keV	$r_{500}^{\rm WL}$	$r_{500}^{\rm WL}$	All	1.97 ± 0.89	1.04 ± 0.06	0.46 ± 0.23
$T_X^{\rm cut}/8$ keV	r_{500}^{X}	r_{500}^{X}	All	1.42 ± 0.19	0.96 ± 0.02	0.17 ± 0.08
$L_X^{\rm cut}E(z)^{-1}$	$r_{500}^{\rm WL}$	$r_{500}^{\rm WL}$	All	0.45 ± 0.10	0.93 ± 0.03	0.35 ± 0.07
$L_X^{\rm cut}E(z)^{-1}$	r_{500}^{X}	r_{500}^{X}	All	0.50 ± 0.06	0.91 ± 0.02	0.26 ± 0.05
$M_{\rm Gas}E(z)$	$r_{500}^{\rm WL}$	$r_{500}^{\rm WL}$	All	1.04 ± 0.10	0.90 ± 0.02	0.15 ± 0.06
			$K_0 < 70$ keV cm^2	0.91 ± 0.20	0.89 ± 0.03	<0.1
			$K_0 > 70$ keV cm^2	1.09 ± 0.13	0.90 ± 0.02	0.18 ± 0.09
			$D_{\rm BCG} < 0.01$ Mpc	0.93 ± 0.13	0.89 ± 0.02	<0.06
			$D_{\rm BCG} > 0.01$ Mpc	1.13 ± 0.18	0.90 ± 0.03	0.22 ± 0.15
$Y_X E(z)^{0.6}$	$r_{500}^{\rm WL}$	$r_{500}^{\rm WL}$	All	0.56 ± 0.07	0.45 ± 0.07	0.22 ± 0.05
			$K_0 < 70$ keV cm^2	0.44 ± 0.14	0.53 ± 0.11	0.24 ± 0.18
			$K_0 > 70$ keV cm^2	0.62 ± 0.10	0.41 ± 0.09	0.21 ± 0.09
			$D_{\rm BCG} < 0.01$	0.48 ± 0.09	0.52 ± 0.08	0.17 ± 0.11
			$D_{\rm BCG} > 0.01$	0.65 ± 0.14	0.36 ± 0.13	0.27 ± 0.17
Relations at other radii						
$T_X^{\rm cut}/8$ keV (keV)	1 Mpc	1 Mpc	All	1.10 ± 0.57	0.80 ± 0.02	0.15 ± 0.11
$L_X^{\rm cut}$	”	”	All	0.23 ± 0.06	0.79 ± 0.02	0.19 ± 0.04
$M_{\rm Gas}$	”	”	All	0.83 ± 0.14	0.90 ± 0.03	0.16 ± 0.10
Y_X	”	”	All	0.40 ± 0.06	0.48 ± 0.05	0.12 ± 0.04
$T_X^{\rm cut}/8$ keV	”	$r_{500}^{\rm WL}$	All	3.04 ± 1.38	1.03 ± 0.08	0.46 ± 0.31
$L_X^{\rm cut}$	”	$r_{500}^{\rm WL}$	All	0.50 ± 0.13	0.96 ± 0.03	0.38 ± 0.07
$M_{\rm Gas}$	”	$r_{500}^{\rm WL}$	All	1.73 ± 0.59	1.20 ± 0.13	0.39 ± 0.18
Y_X	”	$r_{500}^{\rm WL}$	All	0.80 ± 0.15	0.35 ± 0.11	0.28 ± 0.14

Notes. All proxies are fit against $M_{\rm WL}E(z)$ at an aperture of $r_{500}^{\rm WL}$ or $M_{\rm WL}$ at an aperture of 1 Mpc. All masses are in units of $10^{14}M_\odot$. The core-cut X-ray luminosity is in units of 10^{45} erg s^{-1}, and Y_X is in units of $10^{14}M_\odot$ keV.